






## RESEARCH ARTICLE

10.1029/2021JD034983

# The Role of Eyewall Turbulent Transport in the Pathway to Intensification of Tropical Cyclones

Ping Zhu<sup>1</sup> , Andrew Hazelton<sup>2,3</sup>, Zhan Zhang<sup>4</sup>, Frank D. Marks<sup>3</sup> , and Vijay Tallapragada<sup>4</sup> 

### Key Points:

- A stability correction that considers cloud effect is added in the turbulence scheme used in the Hurricane Analysis and Forecast System
- The stability correction substantially improves the model's skill in predicting track and intensity of tropical cyclones
- The turbulent transport in the eyewall plays a pivotal role in initiating a positive feedback underlying the storm rapid intensification

<sup>1</sup>Department of Earth and Environment, Florida International University, Miami, FL, USA, <sup>2</sup>Cooperative Institute for Marine and Atmospheric Studies, University of Miami, Miami, FL, USA, <sup>3</sup>Hurricane Research Division, Atlantic Oceanographic and Meteorological Laboratory, NOAA, Miami, FL, USA, <sup>4</sup>Environmental Modeling Center, National Centers for Environmental Prediction, NOAA, Miami, FL, USA

### Correspondence to:

P. Zhu,  
zhup@fiu.edu

### Citation:

Zhu, P., Hazelton, A., Zhang, Z., Marks, F. D., & Tallapragada, V. (2021). The role of eyewall turbulent transport in the pathway to intensification of tropical cyclones. *Journal of Geophysical Research: Atmospheres*, 126, e2021JD034983. <https://doi.org/10.1029/2021JD034983>

Received 29 MAR 2021  
Accepted 13 AUG 2021

### Author Contributions:

**Conceptualization:** Ping Zhu  
**Data curation:** Ping Zhu, Andrew Hazelton, Zhan Zhang  
**Formal analysis:** Ping Zhu, Andrew Hazelton, Zhan Zhang  
**Funding acquisition:** Ping Zhu  
**Investigation:** Ping Zhu, Andrew Hazelton  
**Methodology:** Ping Zhu  
**Project Administration:** Ping Zhu  
**Resources:** Ping Zhu, Andrew Hazelton, Frank D. Marks, Vijay Tallapragada  
**Software:** Ping Zhu  
**Supervision:** Ping Zhu, Frank D. Marks, Vijay Tallapragada

**Abstract** In a tropical cyclone (TC), turbulence not only exists in the planetary boundary layer (PBL) but also can be generated above the PBL by the cloud processes in the eyewall and rainbands. It is found that the Hurricane Analysis and Forecast System (HAFS), a new multi-scale operational model for TC prediction, fails to capture the intense turbulent mixing in eyewall and rainband clouds due to a poor estimation of static stability in clouds. The problem is fixed by including the effects of multi-phase water in the stability calculation. Simulations of 21 TCs and tropical storms in the North Atlantic basin of 2016–2019 hurricane seasons totaling 118 forecast cycles show that the stability correction substantially improves HAFS's skill in predicting storm track and intensity. Analyses of HAFS's simulations of Hurricane Michael (2018) show that the positive tendency of vortex's tangential wind resulting from the radially inward transport of absolute vorticity dominates the eddy correlation tendencies induced by the model-resolved asymmetric eddies and serves as a main mechanism for the rapid intensification of Michael. The sub-grid scale (SGS) turbulent transport above the PBL in the eyewall plays a pivotal role in initiating a positive feedback among the eyewall convection, mean secondary overturning circulation, vortex acceleration via the inward transport of absolute vorticity, surface evaporation, and radial convergence of moisture in the PBL. Without the SGS transport above the PBL, the model-resolved vertical transport alone may not be sufficient in initiating the positive feedback underlying the rapid intensification of TCs.

**Plain Language Summary** Turbulence is commonly regarded as a flow feature pertaining to the planetary boundary layer (PBL), the lowest layer of the atmosphere with a typical depth of 1 km. In fair-weather conditions, the turbulent PBL is cleanly separated from the free atmosphere above by an inversion. In tropical cyclones (TCs), however, intense turbulence can be generated by the cloud-induced buoyancy and extends all the way up to the tropopause in the eyewall and rainbands. In this study, we found that the Hurricane Analysis and Forecast System (HAFS), a new multi-scale operational model for TC prediction expected to be in full operational implementation likely in 2023, is unable to capture the vertical turbulent transport above the PBL in eyewall and rainbands due to a poor estimation of static stability that neglects the buoyancy induced by clouds. This problem is fixed by including the effects of multi-phase water (vapor, liquid and solid hydrometeors) in the stability calculation. The stability correction substantially improves HAFS's skill in predicting storm track and intensity. It is found that the sub-grid-scale turbulent transport above the PBL in the eyewall plays a pivotal role in initiating a positive feedback underlying the rapid intensification of a TC.

## 1. Introduction

Tropical cyclones (TCs) pose a significant risk to loss of life and damage in properties in coastal areas. Yet, an accurate prediction of storm intensity change remains the most difficult challenge in operational forecast of TCs. Improving TC intensity forecast has been one of the highest priorities of the National Hurricane Center (NHC, Kaplan et al., 2015) and one of the focuses of NOAA's Hurricane Forecast Improvement Program (HFIP; Toepfer et al., 2010). The state-of-the-art three-dimensional (3D) full physics operational models in particular have problems in predicting TC rapid intensification (RI), a significant increase in storm intensity in a short period. Studies show (e.g., Kaplan et al., 2015) that consensus models and statistical classification models are more skillful than the 3D full physics dynamical models in predicting RI for

© 2021. The Authors.  
This is an open access article under the terms of the [Creative Commons Attribution License](https://creativecommons.org/licenses/by/4.0/), which permits use, distribution and reproduction in any medium, provided the original work is properly cited.

**Validation:** Ping Zhu, Andrew Hazelton, Zhan Zhang  
**Visualization:** Ping Zhu  
**Writing – original draft:** Ping Zhu  
**Writing – review & editing:** Ping Zhu, Andrew Hazelton, Zhan Zhang, Frank D. Marks, Vijay Tallapragada

multiple thresholds (20 KT/12h, 30 KT/24h, 45 KT/36h, and 55 KT/48h). It remains unclear why a 3D full physics model with sufficient resolution and appropriate data assimilation does not possess the expected skill in predicting RI, and this is an important problem to explore.

One of the weakest links is the parametric representation of model physics, in particular, the turbulent and microphysical processes in the inner-core region of a TC. In a real TC, microphysical processes directly interact with the dynamical processes including the coherent convective up-/down-drafts and turbulent eddies in clouds to generate the diabatic heating and cooling that affect the rate of TC intensification. In numerical simulations, the realization of the complicated microphysical-dynamical interaction depends on how the sub-grid-scale (SGS) processes are parameterized and how they interact with the model-resolved fields. The poor intensity forecasting skill of operational models to simulate RI storms suggests that the interplay between inner-core turbulent and microphysical processes are not appropriately represented in models.

Zhu et al. (2019) showed that a part of the problem is associated with the turbulent mixing parameterization in the eyewall. Turbulence is commonly regarded as a flow feature pertaining to the planetary boundary layer (PBL) with a typical depth of 1 km. In the fair-weather conditions, the turbulent PBL is cleanly separated from the free atmosphere above by an inversion. In the eyewall and rainbands of a TC, however, intense turbulent mixing generated by the cloud processes can extend well above the PBL up to the tropopause (e.g., Giangrande et al., 2013; Hogan et al., 2009; LeMone & Zipser, 1980; Lorsolo et al., 2010; Marks et al., 2008). Using simulations by the Hurricane Weather Research & Forecasting (HWRF) model, Zhu et al. (2019) showed that some poor simulations of RI storms can be attributed to the lack of consideration of eyewall in-cloud turbulent mixing, which virtually removes the microphysics-turbulence interaction in eyewall clouds. Incorporating a simple in-cloud turbulent mixing parameterization in the vertical turbulent mixing scheme (also known as the PBL scheme) notably improves HWRF's skills on predicting RI of major hurricanes. While the importance of parameterization of eyewall SGS turbulent mixing to numerical prediction of TC intensification has been clearly demonstrated, there are unaddressed questions. These include (a) how can the existing turbulent mixing schemes used in the operational models be remediated so that they can appropriately account for the vertical turbulent transport within and above the PBL in the eyewall? and (b) how does the eyewall turbulent transport above the PBL affect the pathway to TC intensification? In this study, we extend our research to the Hurricane Analysis and Forecast System (HAFS), a new multi-scale model and data assimilation package capable of providing operational forecasts of TC track, intensity (including RI), and inner-core structure out to 7 days. HAFS is expected to be in full operational implementation likely in 2023. The major objectives of this paper are: (a) identifying the problem inherent in the vertical turbulent mixing scheme used in the operational HAFS; (b) improving turbulent mixing scheme so that it can appropriately account for the vertical turbulent transport in eyewall clouds to generate robust dynamical-microphysical interaction in TC inner-core region; (c) exploring the role of eyewall turbulent transport in the pathway to RI in full physics numerical simulations. This paper is organized as follows. Section 2 provides a brief review of the HAFS model and illustrates its problem of not being able to generate vertical turbulent transport above the PBL in the eyewall and rainbands. Section 3 discusses how to correctly determine the static stability in eyewall and rainband clouds so that the vertical turbulent mixing scheme can appropriately account for the cloud-induced buoyancy production of turbulence. Section 4 presents the validation of the forecasted tracks and intensities for 21 storms in the North Atlantic basin of 2016–2019 hurricane seasons by the HAFS with the default turbulent mixing scheme and the scheme that incorporates the static stability correction resulting from the cloud-induced buoyancy. In Section 5, using the HAFS's simulations of Hurricane Michael (2018), we explore the role of eyewall vertical turbulent transport in the pathway to Michael's RI. This is followed by a summary in Section 6.

## 2. HAFS Model and Its Vertical Turbulent Mixing Scheme

The model used in this study is a global-nested version of HAFS (HAFS-globalnest). It uses Geophysical Fluid Dynamics Laboratory (GFDL) finite-volume dynamic core (FV3, e.g., Harris & Lin, 2013; Lin, 2004) with a static nest covering most of the Atlantic basin. The grid spacing of the global domain is ~13 km and the grid spacing of the nest is ~3 km for the Atlantic grid layout (Hazelton, Zhang, et al., 2021). There is a 2-way feedback between the parent and nested domains. There are 64 levels in the vertical, the same

as that in the operational Global Forecast System (GFS). The model is initialized with the GFS analysis, and therefore, it can be initialized at 00, 06, 12, and 18 UTC. HAFS-globalnest does not feature ocean coupling. This capability is currently under development. But the surface layer scheme considers the variation of surface exchange coefficients at high wind speeds for oceanic conditions (Bender et al., 2007). HAFS-globalnest has been used in near-real-time experiments (Hazelton, Zhang, et al., 2021), showing promising track skill compared to other operational models, and some skill in predicting TC structure and intensity changes. It has also been utilized in research to understand the processes underlying the intensification of Hurricanes Dorian (2019, Hazelton, Alaka, et al., 2021) and Michael (2018, Hazelton et al., 2020). Gopalakrishnan et al. (2021) also uses the HAFS-globalnest to understand how modifying eddy diffusivity in the PBL schemes affects TC structure and intensity.

The physics used in HAFS-globalnest are similar to those used in the operational GFS, including the GFDL microphysics scheme (Chen & Lin, 2013), RRTMG radiation (Iacono et al., 2008), and the scale-aware-SAS (Han et al., 2017) convection parameterization, which is turned on for the global domain but not the nested domain. Since the grid resolution of the nested domain falls in the so-called gray-zone, whether the convection scheme should be turned on or off will be explored in our future study. The default PBL scheme used in the HAFS-globalnest is the Eddy-Diffusivity-Mass-Flux (EDMF) scheme (Han et al., 2016), which is a first-order K-closure scheme originally formulated by Hong and Pan (1996). Over the years there are many improvements to the PBL scheme, such as the modification to the eddy diffusivity in high wind speed environments (Wang et al., 2018), but the basic formulae used to determine eddy exchange coefficients are kept the same as those in Hong and Pan (1996). Specifically, the eddy momentum exchange coefficient within the PBL is calculated as:

$$K_m = \kappa \frac{u_*}{\phi_m} \alpha z \left(1 - \frac{z}{h}\right)^2, \quad (1)$$

where  $\kappa$  is the von Karman constant;  $u_*$  is the friction velocity;  $z$  is the height above the ground,  $\phi_m$  is the surface layer stability function defined by Businger et al. (1971);  $h$  is a diagnosed scale height for PBL from the bulk Richardson number over the PBL depth and the buoyancy of surface-driven thermals; and  $\alpha$  ( $0 < \alpha < 1$ ) is a tunable coefficient introduced by Gopalakrishnan et al. (2013) to reduce eddy viscosity in TC simulations to match the turbulent observations collected in TCs (Zhang, Marks, et al., 2011). Above the diagnosed PBL height,  $K_m$  is calculated as:

$$K_m = l^2 f_m(R_i) S, \quad (2)$$

where  $l$  is the mixing length;  $S = \sqrt{(|\partial \bar{u} / \partial z|)^2 + (|\partial \bar{v} / \partial z|)^2}$  is the vertical wind shear;  $\bar{u}$  and  $\bar{v}$  are the model-resolved horizontal wind components;  $f_m(R_i)$  is a stability function of gradient Richardson number defined as  $R_i = N^2/S^2$ ;  $N^2$  is the Brunt-Väisälä frequency (BVF). In this scheme, it is calculated as,

$$N^2 = \frac{g}{\bar{\theta}_v} \frac{\partial \bar{\theta}_v}{\partial z}, \quad (3)$$

where  $\bar{\theta}_v$  is the model-resolved virtual potential temperature and  $g$  is the gravity. Once  $K_m$  is determined, the eddy exchange coefficient for heat and moisture is calculated by  $K_{t,q} = K_m P_r^{-1}$ , where  $P_r$  is the Prandtl number. Despite the simplicity of the scheme, a turbulence parameterization above the PBL based on the Richardson number is physically sound since presumably  $R_i$  provides an ideal measure of the expected turbulence generated by the buoyancy and shear production. The scheme is also attractive for operational models as it does not require much computational resource. The key is how to accurately determine the static stability  $N^2$  that determines the buoyancy production of turbulence, provided that  $S$  is available from the model-resolved wind fields.

### 3. Static Stability in the Eyewall and Rainbands

We examined the eddy exchange coefficients in the HAFS-globalnest simulations and found that the default PBL scheme is unable to generate turbulent mixing above the PBL in the eyewall and rainbands. As an example, Figure 1 shows the horizontal plane distribution of the HAFS-globalnest simulated  $K_m$  at

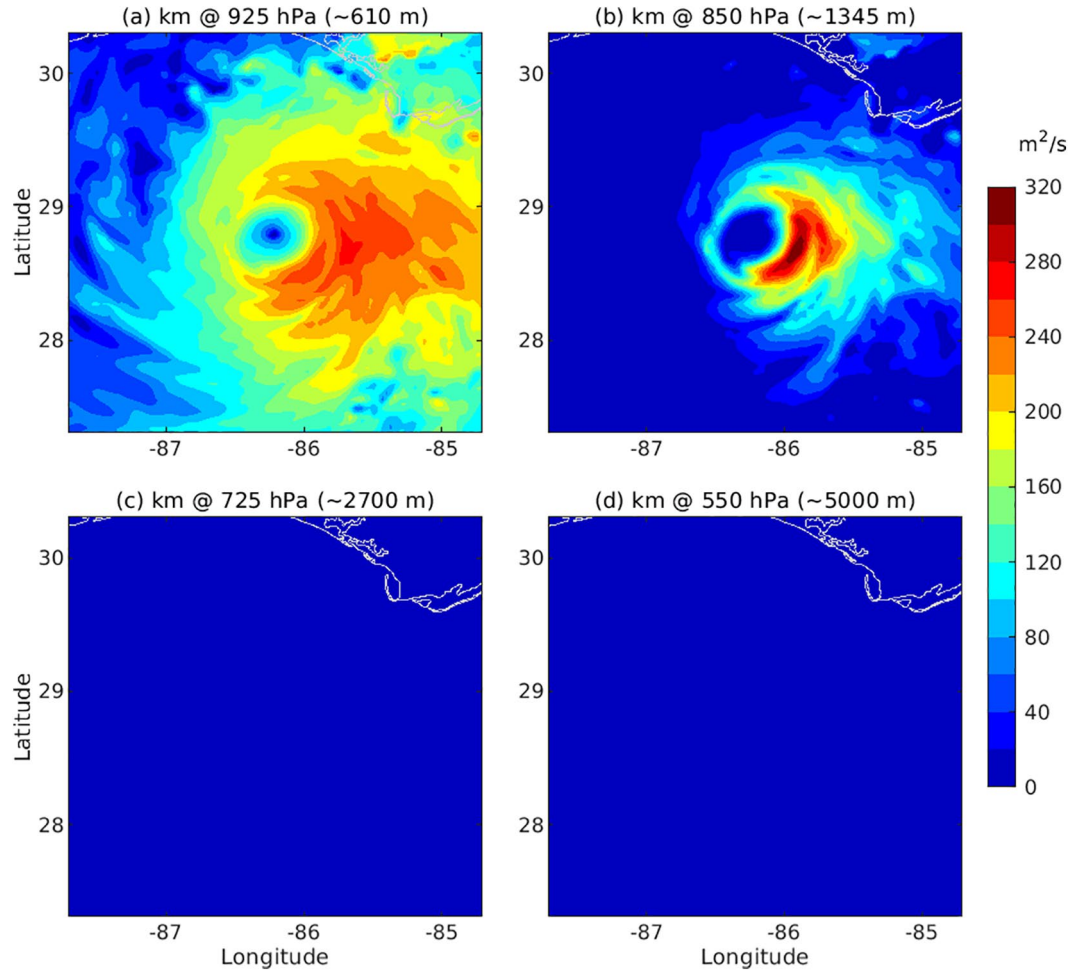


**Figure 1.** Horizontal distribution of eddy momentum exchange coefficients ( $K_m$ ) at the pressure levels of 925, 850, 725, and 550 hPa from a Hurricane analysis and forecast system (HAFS)-Globalnest simulation of Hurricane Michael (2018) at 09:00 UTC, October 10, 2018 during Michael's rapid intensification (RI).

different altitudes of Hurricane Michael (2018) at an arbitrary time before the storm reached its maximum intensity. Within the PBL, the magnitude and spatial distribution of  $K_m$  reflects well the strong turbulent mixing in the eyewall and rainbands, but above the PBL, the HAFS-globalnest generated  $K_m$  is virtually zero, suggesting that the model fails to capture the vertical turbulent transport above the PBL in the eyewall and rainbands. This problem is caused by the inappropriate estimation of static stability in the eyewall and rainbands using Equation 3 because the formula is valid only for the unsaturated atmosphere. As shown in Figure 2a,  $N^2$  at the pressure level of 425 hPa is positive everywhere including the eyewall and rainbands, indicating that Equation 3 generates significant biases of static stability in the deep convective eyewall and rainbands. As a result,  $R_i$  (Figure 2b) is well over the critical Richardson number commonly used for turbulence onset in both TC inner core and outer regions.

The bias of static stability in the eyewall and rainbands can be much reduced if  $N^2$  is calculated using the formula for the saturated atmosphere that contains multi-phase of water including vapor and liquid/solid hydrometeors as,

$$N^2 = g \left\{ \left( 1 + \frac{l_m \bar{q}_s}{R_d \bar{T}} \right) \frac{1}{\bar{T}} \left( \frac{\partial \bar{T}}{\partial z} + \Gamma_m \right) - \frac{1}{1 + \bar{q}_t} \frac{\partial \bar{q}_t}{\partial z} \right\}, \quad (4)$$

where  $\Gamma_m$  is the moist adiabatic lapse rate expressed as,

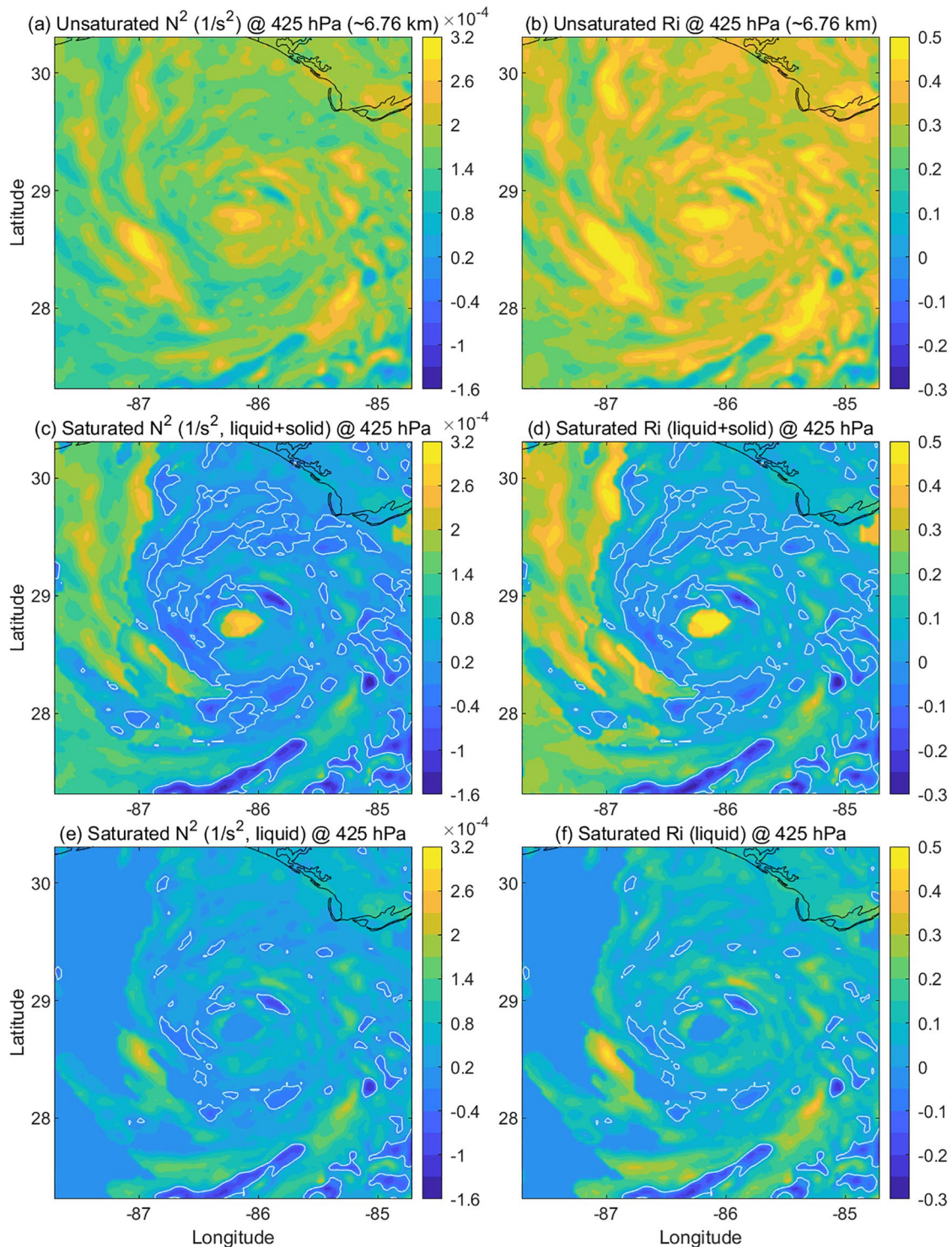


**Figure 2.** (a), (c), and (e): Brunt-Väisälä frequency calculated by Equation 3 for the unsaturated atmosphere, by Equations 4 and 5 for the saturated atmosphere with mixed-phase clouds, and by Equations 6 and 7 treating cloud condensates as “all liquid” at the pressure level of 425 hPa ( $\sim 6.76$  km in altitude) respectively from a HAFS-Globalnest simulation of Hurricane Michael (2018) at 09:00 UTC, October 10 during Michael’s RI. (b), (d) and (f): The corresponding  $R_i = N^2/S^2$ . White contours in (c), (d), (e), and (f) indicate zero value of  $N^2$  and  $R_i$ .

$$\Gamma_m = \frac{g}{C_{pd}} \cdot \frac{(1 + \bar{q}_t) \left( 1 + \frac{l_s \bar{q}_s}{R_d \bar{T}} \right) + \frac{l_f}{g} \frac{\partial \bar{q}_w}{\partial z}}{1 + \frac{C_{pv} \bar{q}_s + C_w \bar{q}_w + C_i \bar{q}_i}{C_{pd}} + \frac{(\epsilon + \bar{q}_s) l_s l_m \bar{q}_s}{C_{pd} R_d \bar{T}^2}}. \quad (5)$$

A derivation of Equations 4 and 5 and the definition of the symbols can be found in Appendix A. For the saturated atmosphere with only liquid hydrometeors, no water phase change associated with freezing and sublimation is involved, then, Equations 4 and 5 reduce to,

$$N^2 = g \left\{ \left( 1 + \frac{l_v \bar{q}_s}{R_d \bar{T}} \right) \frac{1}{\bar{T}} \left( \frac{\partial \bar{T}}{\partial z} + \Gamma_m \right) - \frac{1}{1 + \bar{q}_t} \frac{\partial \bar{q}_t}{\partial z} \right\}, \quad (6)$$

$$\Gamma_m = \frac{g}{C_{pd}} \cdot \frac{(1 + \bar{q}_t) \left( 1 + \frac{l_v \bar{q}_s}{R_d \bar{T}} \right)}{1 + \frac{C_{pv} \bar{q}_s + C_w \bar{q}_w}{C_{pd}} + \frac{(\epsilon + \bar{q}_s) l_v^2 \bar{q}_s}{C_{pd} R_d \bar{T}^2}}. \quad (7)$$

Equations 6 and 7 are the same as those in Durran and Klemp (1982, c.f., Equations 5 and 19 in their paper). The impact of cloud-induced buoyancy on convection simulations has been investigated by a number of studies (e.g., Bretherton & Park, 2009; Han & Bretherton, 2019; Schubert et al., 1979). To our knowledge, there has been no study to date to discuss how the cloud-induced buoyancy affects the turbulent mixing parameterization in the eyewall and how the resultant turbulent transport in eyewall clouds affects the pathway to TC intensification. Moreover, in the previous studies for simplicity hydrometeors were treated either as “all liquid” or “all ice.” We will show shortly that for deep convective eyewall clouds it is important to consider the effect of mixed-phase clouds on static stability.

With the model output, we recalculated  $N^2$  and  $R_i$  using Equations 4 and 5 for the saturated atmosphere that contains mixed-phase hydrometeors. Figures 2c and 2d show the results at the same time and height as those of Figures 2a and 2b. The consideration of the buoyancy induced by clouds substantially reduces the overestimated static stability by  $\left( g / \bar{\theta}_v \right) \left( \partial \bar{\theta}_v / \partial z \right)$ . The horizontal distribution of negative  $N^2$  and  $R_i$  (indicating the static unstable regime) matches well with the eyewall and rainbands. As a comparison, we also calculated  $N^2$  and  $R_i$  using Equations 6 and 7 by treating cloud condensates as “all liquid” (Figures 2e and 2f). This allows us to evaluate the effects of solid phase hydrometeors on the stability in eyewall clouds above the freezing level. The comparison between Figures 2c–2d and 2e–2f clearly shows that the solid phase hydrometeors notably reduce the static stability in the eyewall and rainbands above the freezing level. This result suggests that failure to consider the ice effect on static stability can substantially affect the fidelity of turbulent mixing parameterization when solid hydrometeors exist above the freezing level in a deep convective environment. Note that in this study only the effects of non-precipitating hydrometeors are considered in the stability calculation. The impact of large-size precipitating droplets on atmospheric stability is a more complicated issue, which will be investigated in our future research.

#### 4. Impact of Eyewall Turbulent Transport on TC Track and Intensity Forecast

To examine how the static stability affects the turbulence parameterization in the eyewall and rainbands and the resultant impact on the TC track and intensity forecasts by the HAFS-globalnest, we upgraded the EDMF PBL scheme with the stability correction. Everything else is the same except that we replaced the model's default calculation of BVF by Equation 3 with Equations 4 and 5 that include the impact of multi-phase water on static stability. Using the default and modified HAFS-globalnest, we simulated 21 storms in the North Atlantic basin of 2016–2019 hurricane seasons. These include major hurricanes (CAT 3–5): Gaston (2016), Matthew (2016), Nicole (2016), Harvey (2017), Irma (2017), Jose (2017), Lee (2017), Maria (2017), Michael (2018), and Dorian (2019); weak hurricanes (CAT 1–2): Hermine (2016), Katia (2017), Helene (2018), Isaac (2018), and Leslie (2018); and tropical storms (TS): Gordon (2018), Joyce (2018), Nadine (2018), Erin (2019), Fernand (2019), and Gabrielle (2019) totaling 118 forecast cycles. While we were lim-

ited by the availability of computer resources, we wanted to select a range of cases (strong and weak) over the period of 4 years. Therefore, the chosen cases for the HAFS-globalnest simulations are to compromise between those two constraints. The TC tracks and intensities simulated by the modified HAFS-globalnest with the stability  $N^2$  correction (HAFN, hereafter) and the baseline HAFS-globalnest with the default model physics (HAFB, hereafter) are then compared with the National Hurricane Center (NHC) best-track data.

The overall performance of 5-days track forecasts is summarized in Figure 3. The stability correction shows a consistent improvement on the storm track forecasts. It reduces the absolute track error (defined as the absolute distance between the simulated TC center position and that of the best-track data) by  $\sim 15$  Nautical miles (n mi) by the end of the 5-days forecast (Figure 3a). The decomposition of the absolute track error into the along-track and cross-track bias (Figures 3b and 3c) shows that the track improvements are mainly from the reduction of the along-track biases. The default HAFB produces large negative along-track biases meaning that the simulated storms move too slow with respect to the best-track data. This negative bias is largely reduced by HAFN.

The statistics of intensity forecasts are shown in Figure 4, where we examined both absolute intensity error (defined as the absolute difference in the maximum wind speeds between the simulated storms and the best-track data) and intensity bias that includes the sign with respect to the best-track data. As shown in Figure 4a, the largest improvement in intensity forecast is seen in the 2–3 days forecasts when the absolute intensity error is reduced by  $\sim 4$ –5 Kt due to the stability correction. Figure 4b further indicates that HAFB under-predicts the storm intensity by  $\sim (-10, -20)$  Kt for 2- to 5-days forecasts. HAFN notably reduces this negative bias down to a range of  $\sim (-5, +5)$  Kt. Such an improvement in wind speed forecast is consistent with the forecast of storm minimum center pressure. HAFB over-predicts pressure by  $\sim (5, 10)$  hPa, and this error is reduced down to  $\sim (-2, 2)$  hPa by HAFN (not shown here).

We also verified the forecasts of TC structure measured by the radius of maximum of wind (RMW), 34-Kt radius, 50-Kt radius, and 64-Kt radius (Figure 5). Since not all storms evaluated in this study reach the intensity of 34 Kt, 50-Kt, and 64-Kt, less forecast cycles are available for these statistical evaluations. HAFB generates large positive biases in RMW. This bias is notably reduced by HAFN, suggesting that the stability correction allows HAFN to produce a better eyewall structure. It is, however, unclear why HAFN produces a larger negative bias in 50-Kt radius by  $\sim 3$  n mi than HAFB considering that HAFN yields smaller bias errors of both 34-Kt and 64-Kt radii. This issue will be further investigated when more samples are generated. In short, the stability correction notably improves the HAFS-globalnest's forecasting skill in almost all key measures commonly used for the evaluation of operational TC forecasts.

## 5. Role of Eyewall Turbulent Transport in the Pathway to TC Intensification

While the improvement in HAFS-globalnest's forecasting skill in track and intensity change due to the stability correction is clearly shown in the simulations of North Atlantic basin TCs, the underlying reason for such an improvement is not fully understood. In this section, we will use the HAFS-globalnest simulations of Hurricane Michael (2018) to further demonstrate the forecasting skill improvement due to stability correction and explore the role of eyewall turbulent transport in the pathway to TC intensification.

Figures 6a–6c compare the storm tracks and intensities of Michael (2018) simulated by HAFB and HAFN initialized at 18:00 UTC October 7 along with the best-track data. Both simulations predict an excellent storm track that matches the best-track data well in the 5-days forecast. The simulated storm starts to deviate from the best-track toward the south after 18:00 UTC October 12. Despite an excellent storm track forecast by HAFB, it under-predicts the observed storm intensity by a large margin. In contrast, HAFN nearly reproduces the best-track intensity. Note that although the storm track and intensity changes in all 5-days forecast are shown in Figures 6a–6c, the analyses presented in the rest of the sections only focus on the RI period from 00 UTC October 9 to 18 UTC October 10 before Michael's landfall. The nearly identical storm tracks before Michael's landfall produced by HAFB and HAFN implies that the storm vortex evolves in the same large-scale environment in both simulations. Indeed, the analyses of large-scale fields indicate that the TC vortex is embedded in the nearly identical environment in the two simulations (not shown here). Then, why does the simulated storm vortex undergo different intensification pathway despite the same external forcing? The underlying reasons will be explored in the rest of this section. We hope that this can

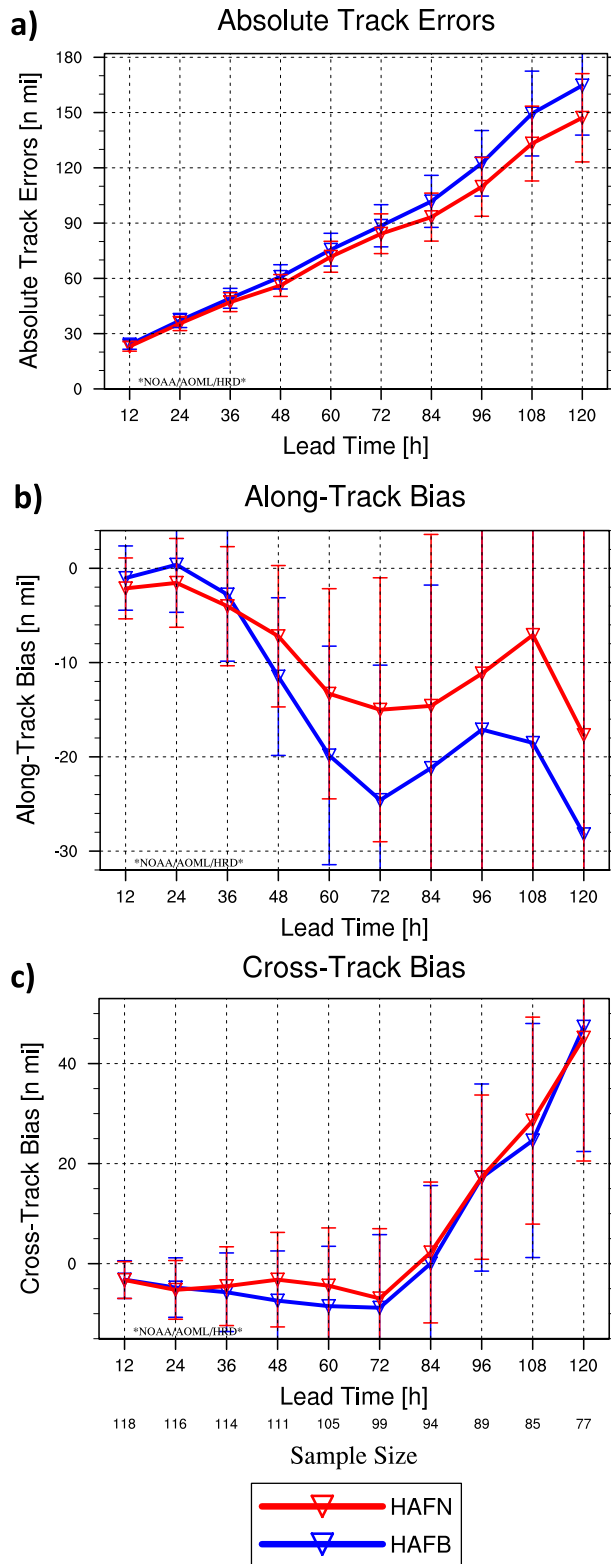
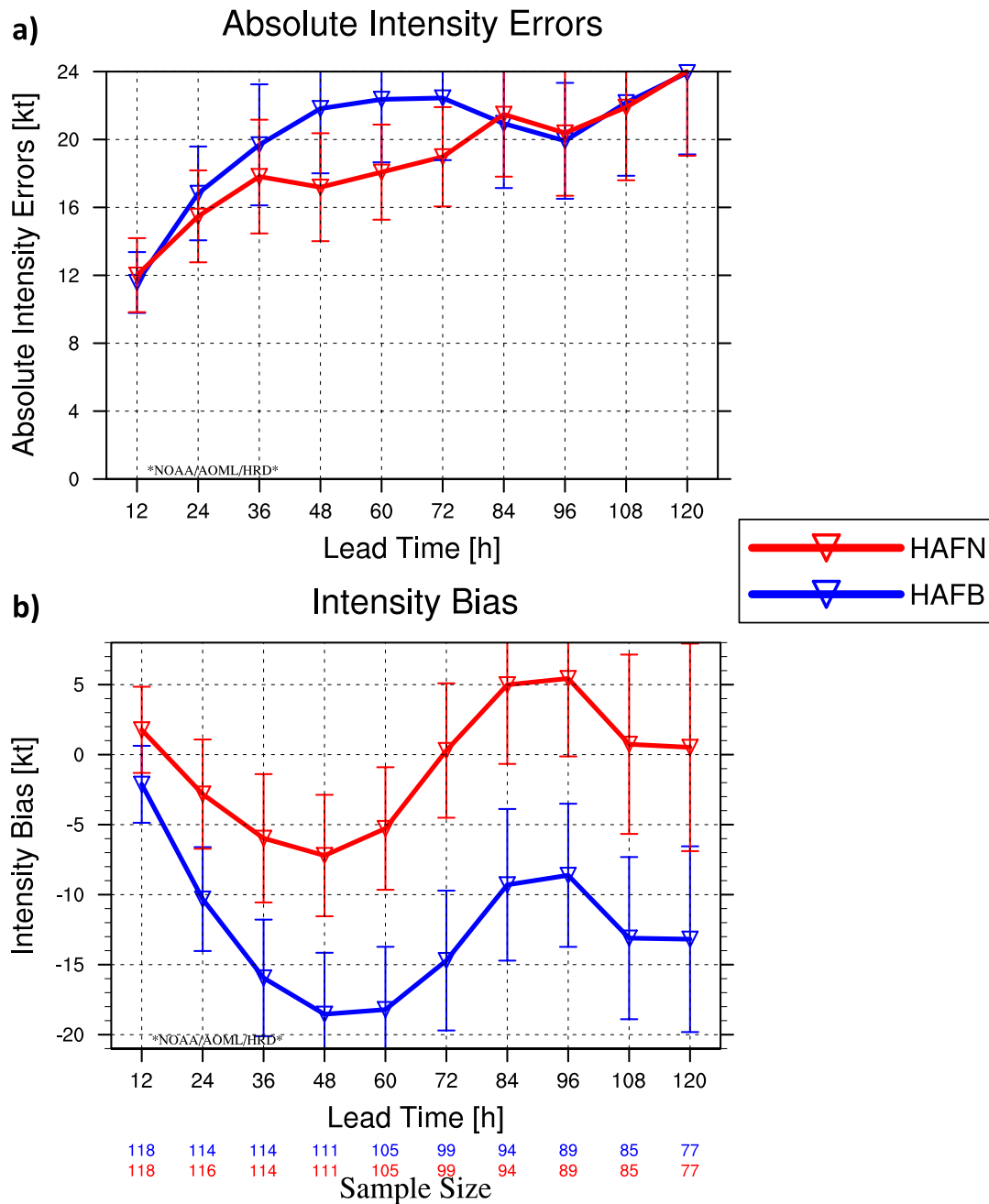


Figure 3.





**Figure 4.** The same as Figure 3 but for bias errors of intensity forecasts by HAFB (blue) and HAFN (red). (a) Absolute intensity errors (Kt) defined as the absolute difference in maximum wind speeds between simulations and best-track data. (b): Intensity biases with respect to the best-track data with sign. The error bars show the 95% confidence interval.

**Figure 3.** Bias errors in Nautical miles (n mi) of track forecasts by Hurricane analysis and forecast system (HAFS)-globalnest as the function of forecast lead time (hours) of 21 storms in the North Atlantic basin of 2016–2019 hurricane seasons. (a): Absolute track errors with respect to the best-track data produced by HAFB (blue) and HAFN (red). (b) and (c): As in (a) but for the along-track and cross-track bias, respectively. Note that the negative (positive) along-track bias indicates the simulated storms are behind (ahead of) the best-track data, whereas the negative (positive) cross-track bias indicates the simulated storms are left (right) to the best-track data. The error bars indicate the 95% confidence interval. The numbers at the bottom of the figure indicate the samples used for the statistics.

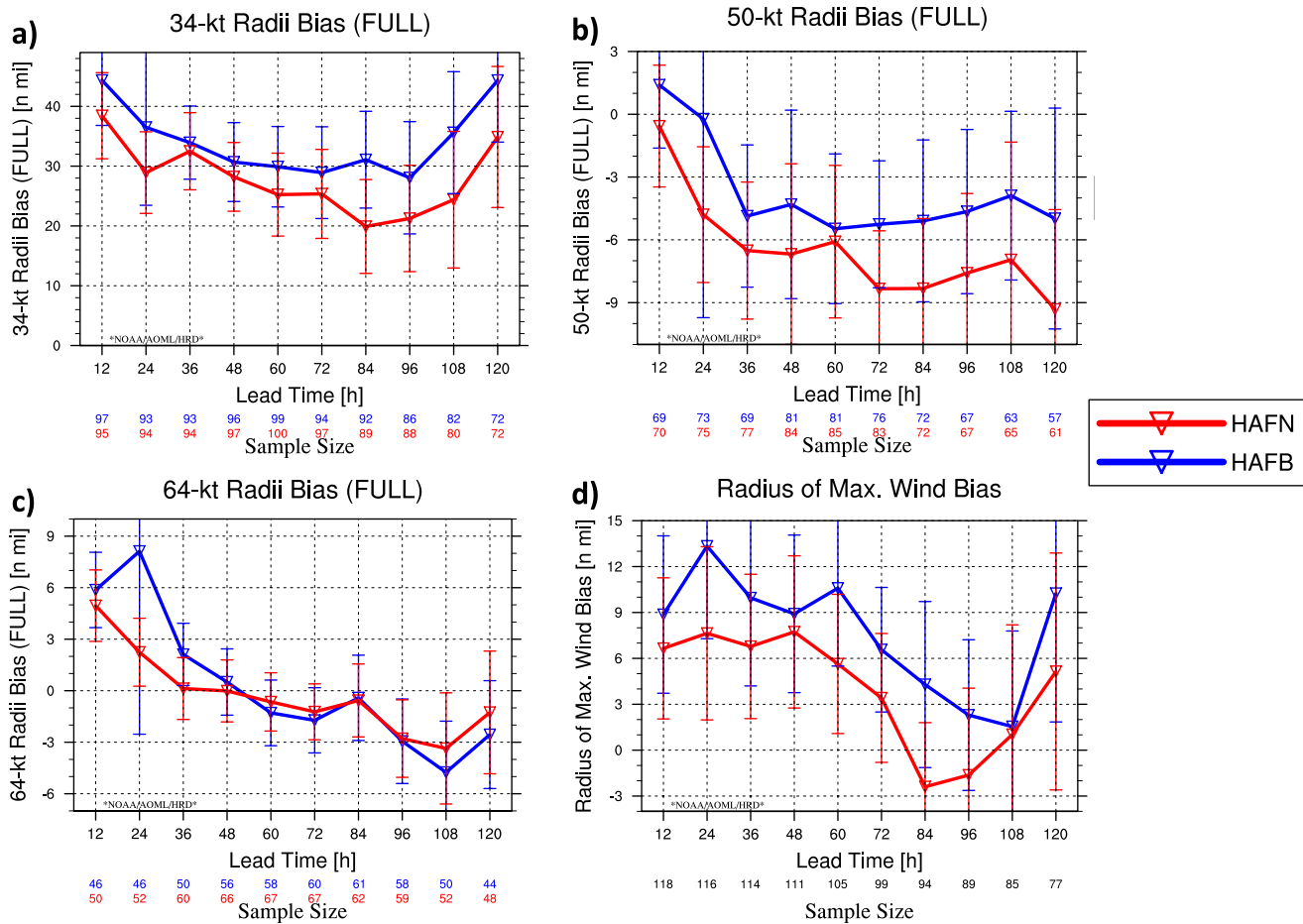


**Figure 5.** The same as Figure 3 but for the forecast bias errors of tropical cyclone (TC) structure measured by (a): 34-Kt radius, (b): 50-Kt radius, (c): 64-Kt radius, and (d) radius of maximum of wind (RMW) as the function of forecast lead time (hours). The error bars show the 95th percent confidence interval.

provide an insight into the vortex intensification governed by the storm internal dynamics and energetics and a guidance for further improvement of intensity forecast skill of HAFS-globalnest.

To examine the fidelity of the vortex inner-core structure simulated by HAFS-globalnest, Figures 6d–6f compare the simulated radar reflectivity of Michael at 09:00 UTC, October 10 with the satellite color image of 85 GHz Polarization corrected brightness temperature (PCT) at 07:37 UTC October 10. This is a time close to the peak intensity of Michael. A well-defined convective ring feature around the storm center is clearly visible in the satellite image (Figure 6d). The eyewall and rainband convection shows a wavenumber-1 asymmetry with the strongest convection to the north and northeast quadrants. HAFN reasonably reproduces the observed inner-core and outer rainband structures including a nearly closed eyewall convective ring, the asymmetric rainbands to the north and northeast quadrants, the long outer rainband tail to the south and southeast quadrants, and the moat in-between the inner and outer rainbands. The asymmetric rainband feature of Michael is also somewhat reproduced by HAFB but with much weaker reflectivity than that of HAFN.

Figure 7 compares the HAFB and HAFN simulated radius-height structure of azimuthal-mean vertical velocity, tangential wind, radial inflow/outflow, radial flow convergence, mixing ratios of sum of cloud, ice, and snow, and rain water averaged over the period from 00:00 UTC October 9 to 18:00 UTC October 10 when Michael underwent its RI. Compared with HAFB, HAFN generates stronger updrafts (color shades in Figure 7b) in the eyewall, stronger radial inflow (red solid contours) within the PBL and outflow (red dashed contours) above, consistent with the stronger tangential winds. In HAFN, the radial flow convergence (white contours in Figure 7d) is strong and matches well with the eyewall updrafts. This feature facilitates

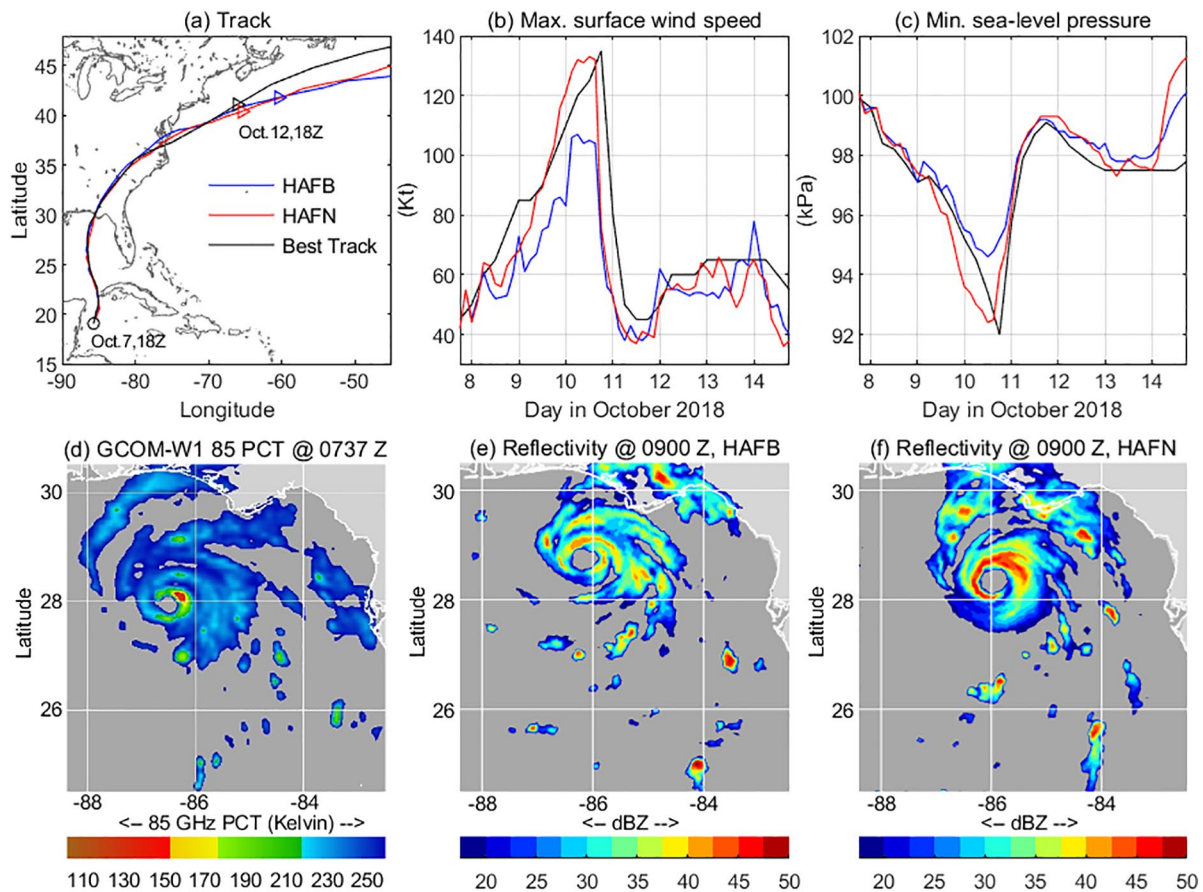


**Figure 6.** (a–c): Track, maximum surface wind speed, and storm central minimum pressure of Michael simulated by HAFB (blue) and HAFN (red) along with the best-track data (Black). Symbols “o” and “Δ” indicate the storm center locations at 18 UTC October 7 and October 12, respectively. (d): Naval Research Laboratory 85 GHz Polarization corrected brightness temperature (PCT) from the Advanced Microwave Scanning Radiometer 2 (AMS2) of GCOM-W1 satellite at 07:37 UTC, October 10. (e and f): Radar reflectivity averaged over the pressure levels of 525–300 hPa at 09:00 UTC, October 10 simulated by HAFB and HAFN, respectively.

an efficient transport of moisture into the eyewall to result in a large amount of condensates (color shading in Figure 7d) in the eyewall. The resultant latent heating fosters the rapid converging spin-up processes as air parcels move radially inward and ascend swiftly within the eyewall. In the meantime, HAFN also generates more precipitation in the inner-core region (red contours in Figure 7d). As discussed by Tyner et al. (2018), the downdrafts resulting from the evaporative cooling of precipitation can effectively uplift the updrafts, leading to the further development of eyewall convection. In contrast, HAFB generates a much weaker radial inflow (Figure 7a) and radial flow convergence (Figure 7c) despite a similar depth of inflow layer to that of HAFN. The weak radial inflow and radial flow convergence are unfavorable to the rapid development of the vortex, since it cannot provide sufficient moisture upward to generate efficient converging spin-up processes. This result suggests that the difference in storm intensity simulated by HAFB and HAFN may be largely attributed to the differences in strength and structure of the secondary overturning circulation resulting from eyewall convection. A more robust microphysical-dynamical interaction in the inner-core region is generated by HAFN during the RI of Michael. The enhanced radial inflow in HAFN leads to greater inward transport of angular momentum in the PBL, which can lead to enhanced spin-up of the vortex (Montgomery & Smith, 2014). This mechanism will be discussed in detail from the tangential wind budget analyses presented shortly.

To further illustrate the impact of stability correction on the vertical turbulent transport in the eyewall, Figure 8 shows the azimuthal-mean vertical profiles of  $N^2$ ,  $R_i$ ,  $K_m$ , buoyancy fluxes, total water fluxes, and

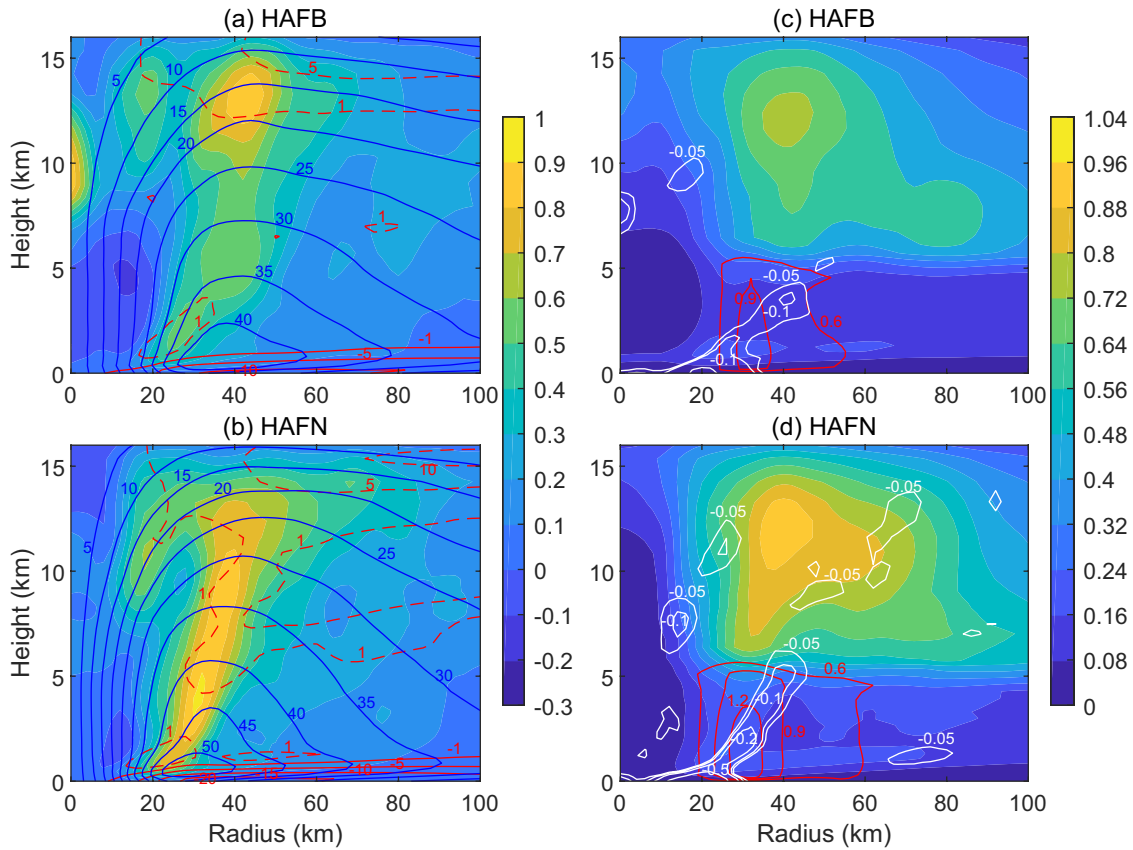


**Figure 7.** (a) and (b): Radius-height structure of azimuthal-mean vertical velocity (color shades  $\text{ms}^{-1}$ ), tangential wind speeds (blue contours from 5 to  $50 \text{ ms}^{-1}$ ), radial inflow (red solid contours with values of  $-1, -5, -10, -15,$  and  $-20 \text{ ms}^{-1}$ ), and radial outflow (red dashed contours with values of  $1, 5,$  and  $10 \text{ ms}^{-1}$ ) averaged over the period from 00 UTC October 9 to 18 UTC October 10 during Michael’s RI simulated by HAFB and HAFN, respectively. (c) and (d): The same as (a) and (b) but for the radial flow convergence (white contours with values of  $-0.2, -0.1,$  and  $-0.05 \text{ s}^{-1}$ ), rain water mixing ratio (red contours with values of  $0.6, 0.9,$  and  $1.2 \text{ gkg}^{-1}$ ), and the sum of cloud, ice and snow mixing ratio (color shades,  $\text{gkg}^{-1}$ ).

momentum fluxes at RMW during Michael’s RI simulated by HAFB and HAFN. The stability correction via Equations 4 and 5 shows a great impact on  $N^2$ ,  $R_i$ , and eddy diffusivity, as well as the vertical buoyancy, total water, and momentum fluxes induced by the model-resolved and parameterized SGS processes. The large total vertical fluxes in HAFN suggest that the stability correction in eyewall clouds yields a robust interaction between the model-resolved and SGS processes leading to the RI of Michael. To examine the effect of hydrometeor phase on atmospheric stability and vertical eddy diffusivity, we calculated two fictitious cases by treating cloud condensates as either “all liquid” or “all ice.” The results are shown by the green dashed and black dashed lines in Figures 8a–8c, respectively. Notable biases of  $N^2$ ,  $R_i$ , and  $K_m$  are shown above and below the freezing level respectively for the two extreme scenarios when condensates are treated as “all liquid” or “all ice.” It suggests that a poor treatment of mixed-phase clouds in the eyewall may lead to incorrect pathways to TC intensification.

The large differences in the azimuthal-mean tangential wind between the two simulations shown in Figures 7a and 7b suggest that the storm intensification may be better understood by looking into the tangential wind tendencies induced by various processes. The azimuthal-mean tangential wind budget equation may be written as,

$$\frac{\partial \bar{v}}{\partial t} = -\bar{u}\bar{\xi} - \bar{w}\frac{\partial \bar{v}}{\partial z} - \overline{u'\zeta'} - v'\frac{\partial v'}{r\partial \lambda} - w'\frac{\partial v'}{\partial z} + D_{\text{sgs-}\lambda}, \quad (8)$$

where  $r, \lambda,$  and  $z$  are the radial, azimuthal, and vertical coordinate axes;  $u, v,$  and  $w$  are the model-resolved radial, tangential, and vertical wind components, respectively; Overbar and prime indicate the azimuthal-mean

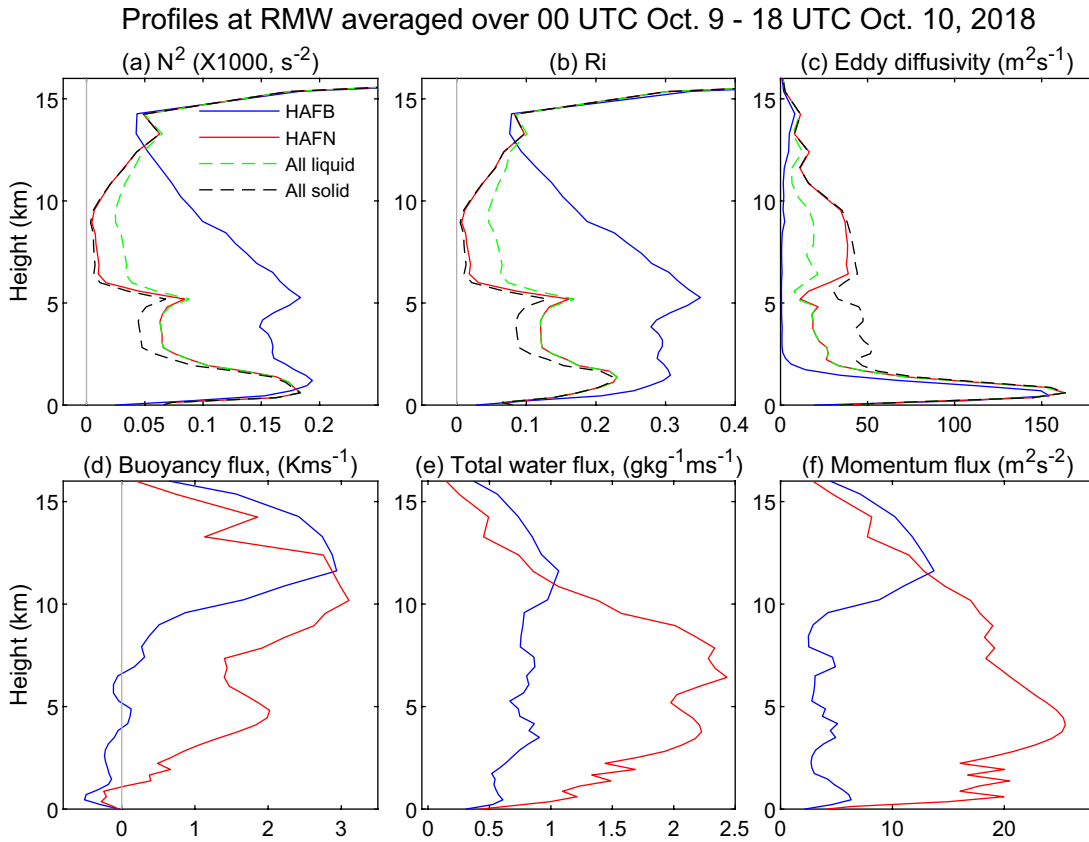


**Figure 8.** Vertical profiles of azimuthal-mean  $N^2$ ,  $R_i$ ,  $K_m$ , buoyancy fluxes, total water fluxes, and momentum fluxes at radius of maximum of wind (RMW) averaged over the period from 00 UTC October 9 to 18 UTC October 10, 2018 simulated by HAFB (blue) and HAFN (red). The fluxes shown in (d–f) include both model-resolved and sub-grid scale (SGS) components. The green dashed and black dashed lines in (a–c) indicate the profiles of  $N^2$ ,  $R_i$ , and  $K_m$  calculated by treating cloud condensates as “all liquid” and “all ice,” respectively.

and the perturbations away from the azimuthal-mean;  $\zeta = (\partial v / \partial r) + (v / r)$  and  $\xi = \zeta + f$  are the relative vorticity and absolute vorticity, respectively;  $f$  is the Coriolis parameter. The first and second terms on the right-hand side (RHS) of Equation 8 represent the tendencies resulting from the radial transport of mean absolute vorticity by the mean radial flow and the vertical advection of mean tangential wind by the mean vertical velocity. These two terms are determined by the interaction between the axisymmetric primary circulation and secondary overturning circulation. The third, fourth, and fifth terms on the RHS of Equation 8 are the tendencies resulting from the radial, tangential, and vertical eddy correlations. These three terms are determined by the model-resolved asymmetric eddies. The last term on the RHS of Equation 8,  $D_{\text{sgs-}\lambda}$ , is the friction dissipation tendency resulting from SGS turbulence and viscosity. Since  $D_{\text{sgs-}\lambda}$  is mainly negative near the surface, in this study we do not explicitly calculate this term, rather, we look for the terms on the RHS of Equation 8 that can result in positive tendencies to overcome the friction dissipation leading to the acceleration of the mean vortex.

From the model output, we calculated the first five terms on the RHS of Equation 8. Here, we first show the detailed budget analyses of Michael simulated by HAFN, and then, compare the results with those from HAFB to reveal the important differences between the two simulations that lead to the different pathways to Michael’s intensification. Figures 9a and 9b show the two tendency terms associated with the mean secondary overturning circulation during Michael’s RI. The radial transport of absolute vorticity ( $-\bar{u}\bar{\xi}$ , color shades) generates large positive and negative tendencies within the inflow and outflow layer, respectively. The peak tendency occurs on the inward side of RMW. This radius-height structure of  $-\bar{u}\bar{\xi}$  is easy to understand from the distribution of mean radial flow (red solid and dashed contours) and absolute vorticity (black contours). Since  $\bar{\xi}$  is positive everywhere, the sign of  $-\bar{u}\bar{\xi}$  is determined by the mean radial flow,

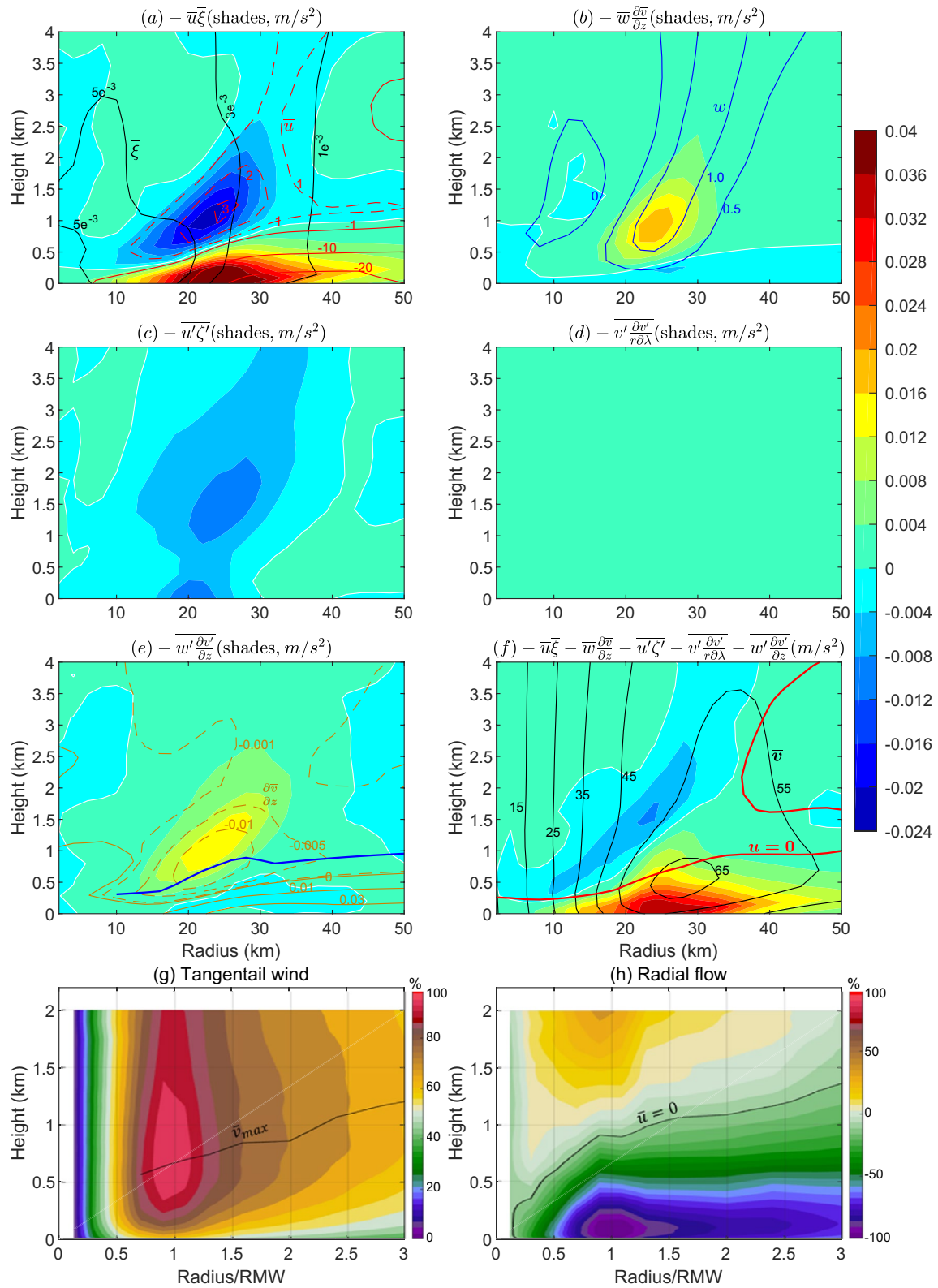
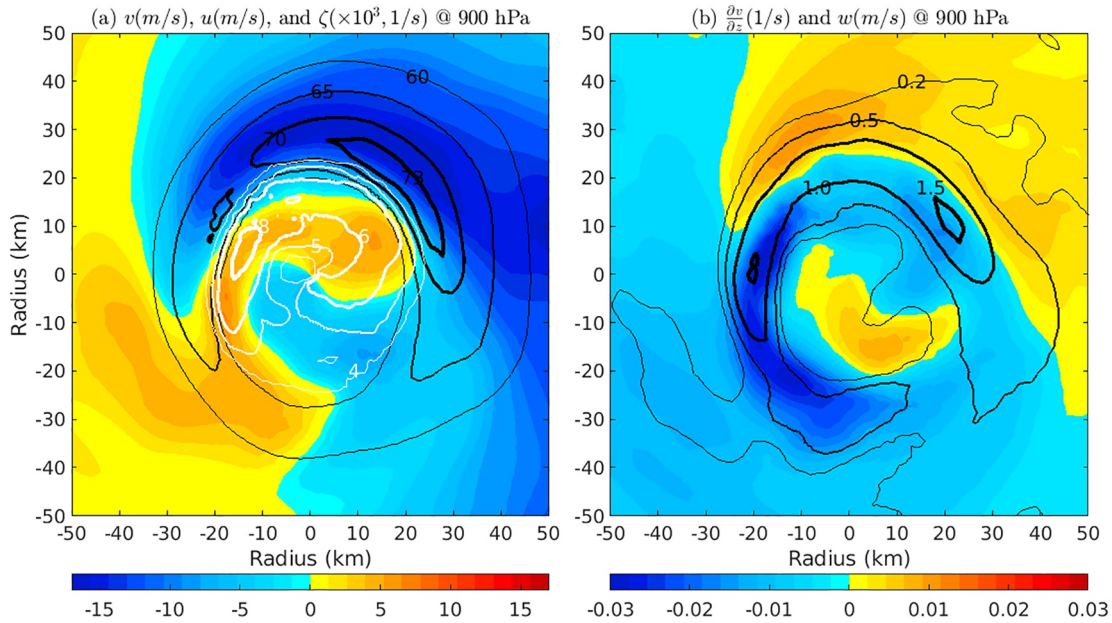


Figure 9.



**Figure 10.** (a): Horizontal plane distribution of tangential wind ( $v$ , black contours, 60, 65, 70, and 73  $\text{ms}^{-1}$ ), radial flow ( $u$ , color shades,  $\text{ms}^{-1}$ ), and relative vorticity ( $\zeta$ , white contours,  $4e^{-3}$ ,  $5e^{-3}$ ,  $6e^{-3}$ , and  $8e^{-3}$   $\text{s}^{-1}$ ) at the pressure level of 900 hPa averaged over the period of 03:00–15:00 UTC October 10 from HAFN. (b): The same as (a) but for  $\partial v / \partial z$  (color shades,  $\text{s}^{-1}$ ) and vertical velocity ( $w$ , black contours, 0.2, 0.5, 1.0, and 1.5  $\text{ms}^{-1}$ ).

yielding positive and negative tendencies of  $-\bar{u}\bar{\zeta}$  in the inflow and outflow layer, respectively. The peak value of  $-\bar{u}\bar{\zeta}$  occurs somewhere between the strongest inflow and maximum  $\bar{\zeta}$  depending on the specific radius-height structure of radial flow and absolute vorticity.

The sign of the tendency induced by  $-\bar{w}(\partial\bar{v}/\partial z)$  can also be easily determined from the radius-height structure of the mean vertical velocity and tangential wind (Figure 9b). Since  $\bar{w}$  is positive in the vicinity of RMW, the sign of  $-\bar{w}(\partial\bar{v}/\partial z)$  is determined by the vertical gradient of tangential wind. Below and above the height of peak tangential wind, which is located just below  $\bar{u} = 0$ ,  $(\partial\bar{v}/\partial z)$  is positive and negative, respectively. Therefore,  $-\bar{w}(\partial\bar{v}/\partial z)$  has an opposite sign to  $-\bar{u}\bar{\zeta}$ , causing the two terms to cancel each other. But since the magnitude of  $-\bar{w}(\partial\bar{v}/\partial z)$  is overwhelmed by  $-\bar{u}\bar{\zeta}$  (Figure 9a vs. 9b), the positive tendency caused by  $-\bar{w}(\partial\bar{v}/\partial z)$  above the height of peak tangential wind will not generate net acceleration of the mean vortex.

The tendencies resulting from the model-resolved asymmetric eddies are shown in Figures 9c–9e, respectively. The tendency induced by  $-\bar{u}\bar{\zeta}'$  is mostly negative throughout the entire vertical column in the inner-core region near RMW (Figure 9c). To better understand this negative tendency of  $-\bar{u}\bar{\zeta}'$ , we examined the horizontal structure of the vortex at different pressure levels. As an illustration, Figure 10a shows the plane distribution of tangential wind, radial flow, and relative vorticity at 900 hPa ( $\sim 850$  m in altitude) averaged over the same period as that of Figure 9c. All three variables show wavenumber-1 asymmetric structures resulting likely from the mean wind shear. The strongest and weakest tangential winds occur in the northeast and south quadrant, respectively (black contours). The largest relative vorticities also occur in the north quadrant but inside of the strongest tangential wind (white contours), reflecting the combined variations of  $v/r$  and  $\partial v/\partial r$  (the two components in  $\zeta$ ). The radial inflow (blue shades) corresponds well with the strong tangential wind. As air converges inward, it must move up to conserve its mass. This causes the radial outflow (orange shades) to occur inside of the radial inflow. As a result, radial flow is somewhat positively

**Figure 9.** Azimuthal-mean tangential wind tendencies (color shades) induced by (a)  $-\bar{u}\bar{\zeta}$ ; (b)  $-\bar{w}(\partial\bar{v}/\partial z)$ ; (c)  $-\bar{u}\bar{\zeta}'$ ; (d)  $-v'(\partial v'/\partial z)$ ; (e)  $-\bar{w}'(\partial\bar{v}'/\partial z)$ ; and (f) the sum of (a)–(e) averaged over the period of 03–15 UTC October 10 simulated by HAFN. The black, red solid, and red dashed contours in (a) are  $\bar{\zeta}$  ( $1e^{-3}$ ,  $3e^{-3}$ , and  $5e^{-3}$   $\text{s}^{-1}$ ) and  $\bar{u}$  ( $-20$ ,  $-10$ ,  $-1$ ,  $1$ ,  $2$ , and  $3$   $\text{ms}^{-1}$ ). The blue contours in (b) are  $\bar{w}$  (0, 0.5, and 1.0  $\text{ms}^{-1}$ ). The brown solid and dashed contours in (e) are  $\partial\bar{v}/\partial z$  (0.03, 0.01, 0,  $-0.001$ ,  $-0.005$ , and  $-0.01$   $\text{s}^{-1}$ ). The thick blue line in (e) denotes the height of minimum  $\partial\bar{v}/\partial z$ . The back and thick red contours in (f) are  $\bar{v}$  (15–65  $\text{ms}^{-1}$ ) and  $\bar{u} = 0$ . The white contour is the contour of zero tendency. (g) and (h): Dropsonde composites of normalized tangential wind and radial flow ( $(\bar{v}/\bar{v}_{\max}), (\bar{u}/|\bar{u}_{\min}|)$ ) as the function of height and normalized radius by RMW from  $\sim 800$  dropsondes collected in 13 TCs (after Zhang et al., 2020).

correlated to the relative vorticity, leading to the negative tendency of  $-\overline{u'\zeta'}$  shown in Figure 9c. Thus, the eddy radial correlation will not accelerate the primary vortex. The calculations show that  $-v'(\partial v'/\partial z)$  (Figure 9d) is much smaller than the other eddy terms, thus, it is negligible in the evolution of a vortex.

As shown in Figure 9e,  $-w'(\partial v'/\partial z)$  generates a positive tendency above the height of maximum tangential wind near RMW, which can be well explained by the plane distribution of the vertical velocity and vertical gradient of tangential wind (Figure 10b). At the pressure level of 900 hPa, which is above the height of the peak tangential wind, the tangential wind decreases with height near RMW. This negative  $\partial v'/\partial z$  (blue color shades) corresponds well with the updrafts (black contours), leading to the positive tendency of  $-w'(\partial v'/\partial z)$ . The radius-height structure of  $-w'(\partial v'/\partial z)$  may also be qualitatively understood from the eddy perturbation argument as follows. Above the height of the minimum  $(\partial \bar{v}/\partial z)$  (thick blue line in Figure 9e) near RMW,  $(\partial \bar{v}/\partial z)$  increases with height (dashed orange contours in Figure 9e). Now considering the perturbation induced by a random eddy. An upward perturbation ( $w' > 0$ ) will yield  $(\partial v'/\partial z) < 0$  since the eddy moves into a new environment that has the larger value of  $\partial \bar{v}/\partial z$  than that of its initial environment before the perturbation. This yields  $w'(\partial v'/\partial z) < 0$ . Likewise, a downward perturbation ( $w' < 0$ ) will yield  $(\partial v'/\partial z) > 0$  as the eddy moves into a new environment that has a smaller value of  $\partial \bar{v}/\partial z$ . This again results in  $w'(\partial v'/\partial z) < 0$ . The net effect of eddy perturbations, thus, is to generate a positive tendency of  $-w'(\partial v'/\partial z)$  regardless of the orientation and magnitude of an eddy perturbation. A similar argument can be applied to the layer below the height of the minimum  $\partial \bar{v}/\partial z$ . An upward ( $w' > 0$ ) or downward ( $w' < 0$ ) eddy perturbation will yield  $(\partial v'/\partial z) > 0$  or  $(\partial v'/\partial z) < 0$ , respectively, to result in a net negative tendency of  $-w'(\partial v'/\partial z)$ . Note that the sign of the actual  $-w'(\partial v'/\partial z)$  calculated from the model output may not exactly follow the previous eddy perturbation argument. This is because the actual value of  $-w'(\partial v'/\partial z)$  involves the complicated 3D feature of a vortex, whereas the eddy perturbation argument is made only from a 1D simplification (upward or downward). Nonetheless, it provides a concise way to understand the contribution of asymmetric eddies to the tendency of a vortex's intensification. As we see here, the eddy induced tangential wind tendency is linked closely to the mean radius-height structure of a vortex.

To understand the contributions of eddy correlation terms to the vortex intensification relatively to the mean secondary circulation, Figure 9f shows the total tendencies induced by the first five terms on the RHS of Equation 8. It clearly shows that the positive tendency above the inflow layer induced by  $-w'(\partial v'/\partial z)$  (Figure 9e) is overwhelmed by the negative tendencies induced by other terms. This leaves the inward transport of absolute vorticity by the mean radial inflow ( $-\bar{u}\zeta$ ) to be the main driving force for the vortex acceleration in this case. As shown in Figure 9f, the largest positive tendency occurs near the surface in the vicinity of RWM, but it is largely canceled out by the negative tendency of friction dissipation (not shown here). The combined effect of  $-\bar{u}\zeta$  and the friction dissipation causes the net acceleration of tangential wind to occur in the upper inflow layer just beneath the surface of  $\bar{u} = 0$ . This result is consistent with the dropsonde observations reported by Zhang, Rogers, et al. (2011), Zhang et al. (2020). Figures 9g and 9h adopted from Zhang, Rogers, et al. (2011), Zhang et al. (2020) show the composite radius-height structure of tangential wind and radial flow normalized by their peak values and RMW from  $\sim 800$  dropsondes collected in 13 TCs in the North Atlantic basin (Detailed information about the dropsonde observations can be found in the references provided). It clearly shows that the maximum tangential wind speed occurs inside the inflow layer just beneath the surface of  $\bar{u} = 0$ . The consistency of radius-height structure of the tangential wind and radial flow between the HAFN simulation and the dropsonde composites supports the conclusion that the radially inward transport of absolute vorticity by the mean secondary circulation is mainly responsible for the vortex acceleration during Michael's RI.

It should be noted that the importance of the mean secondary circulation to TC intensification drawn from the budget analyses here does not conflict with the mechanism of 3D rotating convective updraft paradigm proposed by Montgomery and Smith (2014), which states the importance of asymmetric eddies, such as hot towers, to TC intensification. Persing et al. (2013) showed that the 3D eddy processes associated with vortical plumes can assist the intensification process by contributing to the azimuthally averaged heating rate and to the radial contraction of the maximum tangential velocity. This is consistent with the result of Nolan et al. (2007) who demonstrated that the intensification of a balanced, baroclinic TC-like vortex is mainly driven by the TC sym-



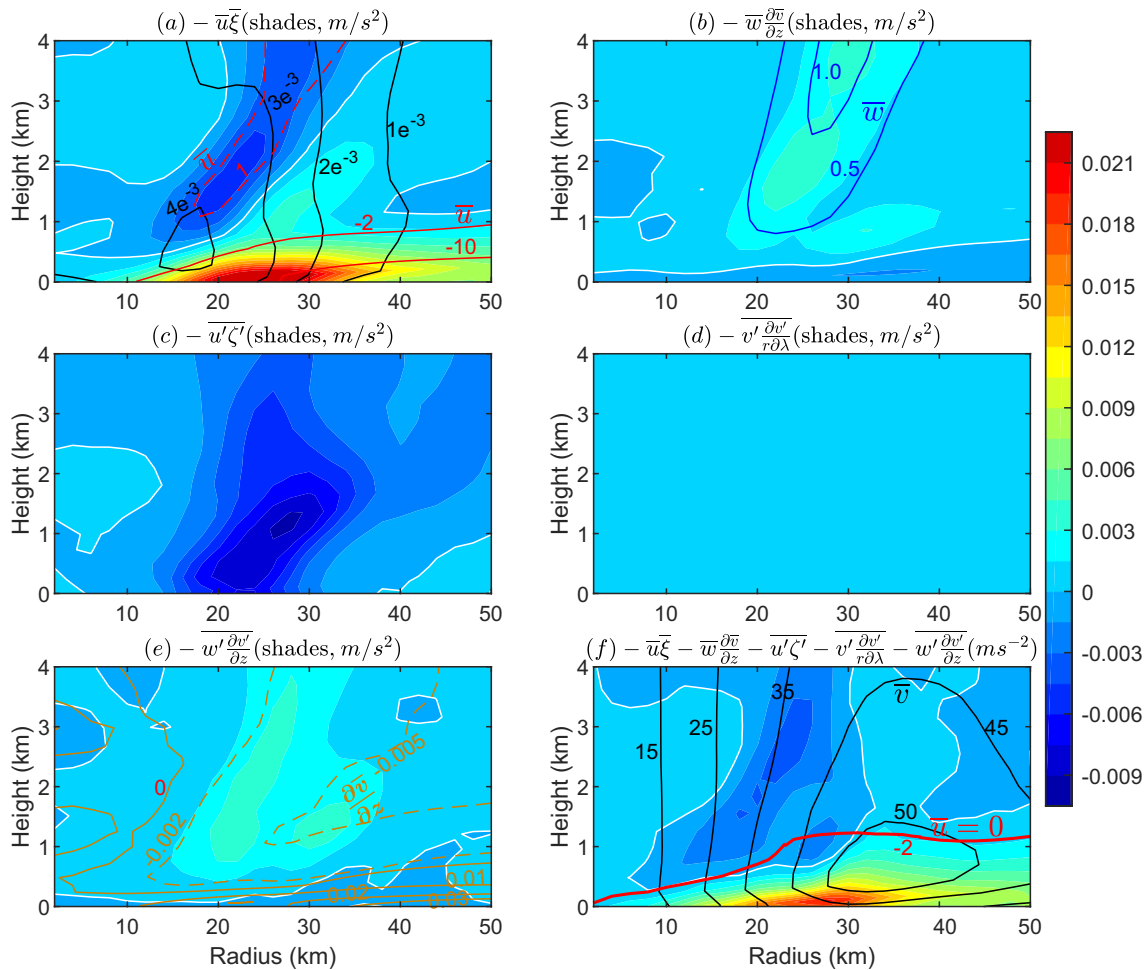


**Figure 11.** The same as Figures 9a–9f but for the tangential wind budget analyses from HAFB.

metric response to the azimuthally averaged diabatic heating, rather than to the heating associated with individual asymmetries distributed around the TC vortex. The detailed interaction between eyewall asymmetric convective elements and the acceleration of the mean vortex circulation will be investigated in our future research.

As a comparison to the tangential wind budget analyses from the HAFN simulation, Figure 11 shows the same budget analyses from the HAFB simulation. Both budget analyses share the same characteristics in that the radial transport of absolute vorticity ( $-\bar{u}\bar{\zeta}$ ) dominates over other tendency terms but it is much weaker in HAFB than in HAFN. To illustrate how this difference affects the vortex evolution during the intensification of Michael (2018), Figure 12a compares the time variation of  $-\bar{u}\bar{\zeta}$  averaged over the radii of (RMW–10, RMW+10) km and below the pressure level of 900 hPa between the two simulations. In HAFN,  $-\bar{u}\bar{\zeta}$  starts to increase before Michael’s RI, and then, jumps into the RI (red line). After that, it stays high throughout the RI period till the landfall of Michael. This large positive tendency induced by the inward transport of absolute vorticity and the resultant increase of tangential wind enhance surface evaporation and radial convergence of moisture in the PBL (Figure 12b, red line), which further fosters stronger eyewall convection evidenced from the increase of vertical velocity (Figure 12c, red line). The enhanced eyewall convection in turn causes the further increase of radial inflow (Figure 12d, red line). The fact that these processes go hand-in-hand suggests that a Wind-Induced Surface Heat Exchange (WISHE, Emanuel, 2003) like positive feedback mechanism has been kicked off, leading to the RI of Michael in the HAFN simulation. In contrast, the positive tendency induced by  $-\bar{u}\bar{\zeta}$  in HAFB (blue line) remains small compared with that in HAFN. Thus, after compensating the friction dissipation and other negative tendencies, the remnant of  $-\bar{u}\bar{\zeta}$  is not sufficiently large to generate the

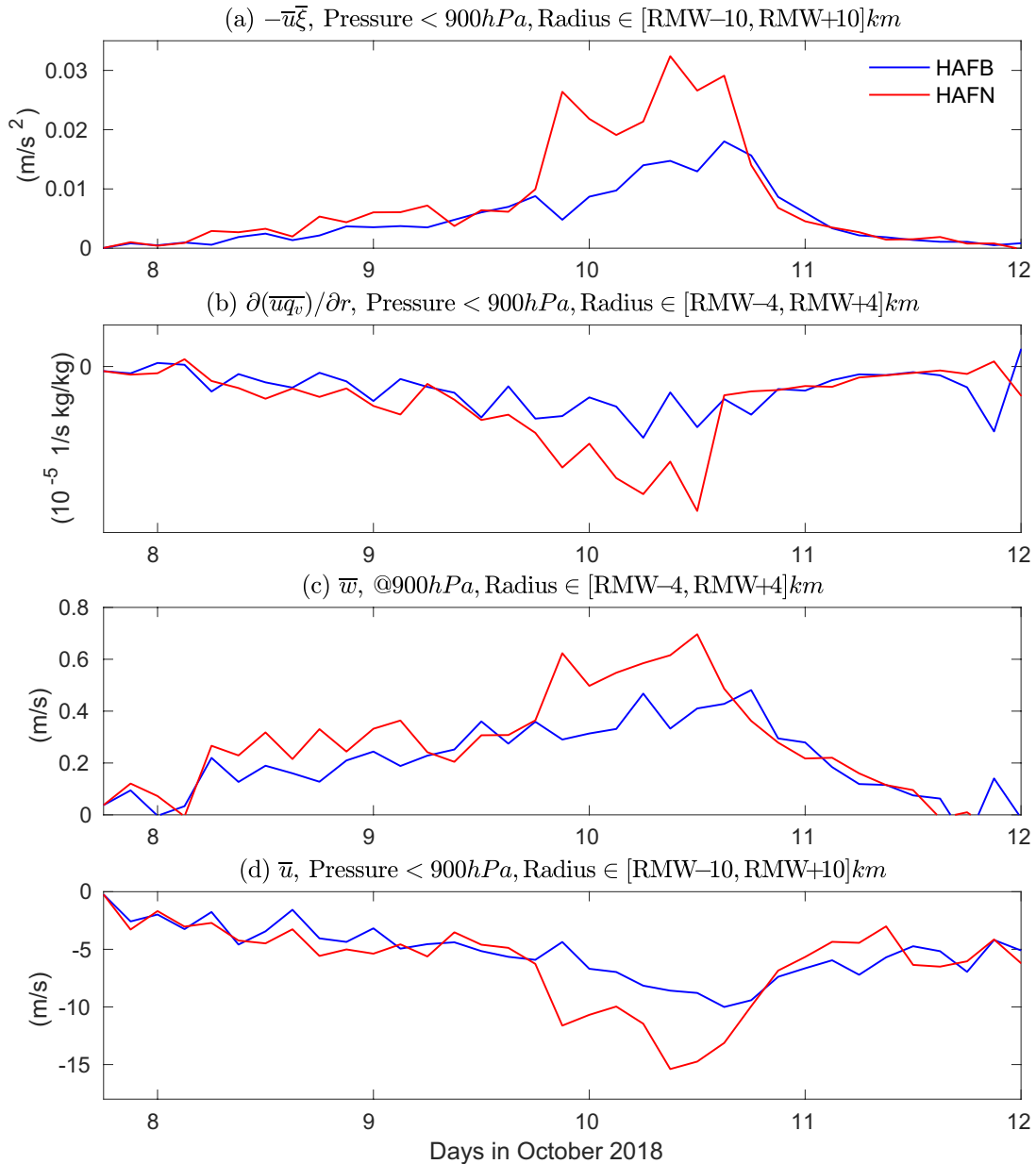


**Figure 12.** Time variations of azimuthal-mean (a) inward transport of absolute vorticity ( $-\bar{u}_z \bar{\xi}$ ); (b) convergence of radial moisture flux  $\partial(\bar{u} \bar{q}_v)/\partial r$ ; (c) vertical velocity  $\bar{w}$ , and (d) radial inflow  $\bar{u}$  averaged over the radii of (RMW-4, RMW+4) km and below the pressure level of 900 hPa from HAFB (blue) and HAFN (red).

needed acceleration of tangential wind to kick off the WISHE-like feedback mechanism underlying the RI of Michael. This result suggests that regardless of the strength of individual convective elements the azimuthal-mean eyewall convection must exceed a critical level so that the induced mean secondary overturning circulation can generate sufficiently large inward transport of absolute vorticity needed for vortex intensification.

One question remains to be answered is why eyewall convection can develop and kick off Michael's RI in HAFN but not in HAFB with the only change in the stability calculation. To answer this question, we examined the vertical moisture transport induced by the model-resolved convection and parameterized SGS turbulent processes. The model-resolved vertical flux of a generic scalar  $\phi$  is commonly calculated as  $w' \phi'$  using the eddy correlation method, where overbar and prime are the domain mean and perturbations away

from the mean. Since HAFS-globalnest is a basin-scale model, when applying this method for estimating fluxes, a domain used for calculating the mean and perturbations needs to be defined. We tested several domains with different sizes and found that the calculated fluxes do not vary substantially as long as the domain covers the entire vortex. The fluxes presented below are calculated from a domain that consists of  $100 \times 100$  model grid points centered at the storm eye, covering an area of  $\sim 300 \times 300 \text{ km}^2$ . Once the domain mean at each model level is determined, the flux at each model grid point is calculated as  $w'\phi'$ . Note that the eddy correlation method was originally designed for estimating fluxes by assuming horizontally homogeneous ambient conditions. But the mean fields of a TC vortex are not horizontally homogeneous. This introduces an uncertainty when applying the eddy correlation method. The related issues of how to accurately quantify the vertical transport in a TC environment will be further investigated in our future research. The vertical fluxes induced by the SGS turbulent process at each model grid are calculated as  $-K(\partial\phi/\partial z)$ , where  $K$  is the eddy diffusivity. Once the model-resolved and SGS fluxes at each model grid are determined, the azimuthal-mean fluxes are calculated by averaging over the rings centered at the storm eye as the function of radius at each model level.

Figures 13a–13d show the radius-height distribution of azimuthal-mean model-resolved and SGS vertical moisture fluxes ( $\overline{w'q'_v}$  and  $-\overline{K_q(\partial q_v/\partial z)}$ ) averaged over an early simulation period before Michael's RI. In the HAFN simulation, there are a large amount of SGS vertical moisture fluxes in the PBL induced by the PBL turbulent processes (Figure 13d). The model-resolved moisture fluxes in the PBL are negligible since 3 km grid resolution of HAFS-globalnest is too coarse to resolve PBL turbulence (Figure 13c). Above the PBL, the static stability correction allows HAFN to generate a significant amount of SGS moisture fluxes that are comparable to the model-resolved moisture fluxes. Because of the combined vertical moisture transport by the model-resolved and SGS processes, the eyewall convection can develop sufficiently strong to generate the needed positive tendency resulting from the inward transport of absolute vorticity to overcome the frictional dissipation and other negative tendencies, leading to the acceleration of vortex's primary circulation as discussed previously. In the HAFB simulation, the PBL scheme also generates a large amount of SGS moisture fluxes in the PBL as expected (Figure 13b), but little turbulence is generated above the PBL because of the incorrect estimation of in-cloud static stability. This suppresses the SGS vertical moisture transport in eyewall and rainband clouds. The moisture transport by the model-resolved processes alone (Figure 13a) is not enough to support the needed convection to kick off the WISHE-like feedback mechanism among the eyewall convection, mean secondary circulation, acceleration of the primary circulation by the inward transport of absolute vorticity, surface evaporation, and radial convergence of moisture in the PBL.

Figures 13e–13h shows the same vertical moisture fluxes but averaged over a later simulation period during Michael's RI. In the HAFN simulation, the radius-height structure of SGS moisture transport remains the same with the magnitude slightly increased compared to the early simulation time (Figures 13d vs. 13h). A key difference from the early simulation time is that the model-resolved moisture fluxes dominate over the SGS moisture fluxes (Figures 13g vs. 13h). It suggests that the SGS processes have successfully helped initiate the WISHE-like positive feedback at the earlier time. Once the pathway is set, the internal interaction among the model-resolved processes can drive the vortex to intensify by itself. In the HAFB simulation, the WISHE-like positive feedback has never really been fully excited without the assistance from the SGS moisture transport above the PBL. This sets up a different pathway for the vortex development in which the internal interaction among the model-resolved processes is unable to generate the sufficiently large inward transport of absolute vorticity to kick off the WISHE-like positive feedback. It is in this context that the role of SGS turbulent transport above the PBL in TC intensification is clear, that is, it helps initiate the WISHE-like positive feedback underlying the RI that sets the intensification pathway for a developing vortex. Note that here we use vertical moisture flux as an example to illustrate the mechanism underlying the RI. In fact, the signature of the positive feedback initiated by the eyewall SGS turbulent transport is also shown in other second-order eddy moments, such as the buoyancy, total water, and momentum fluxes.

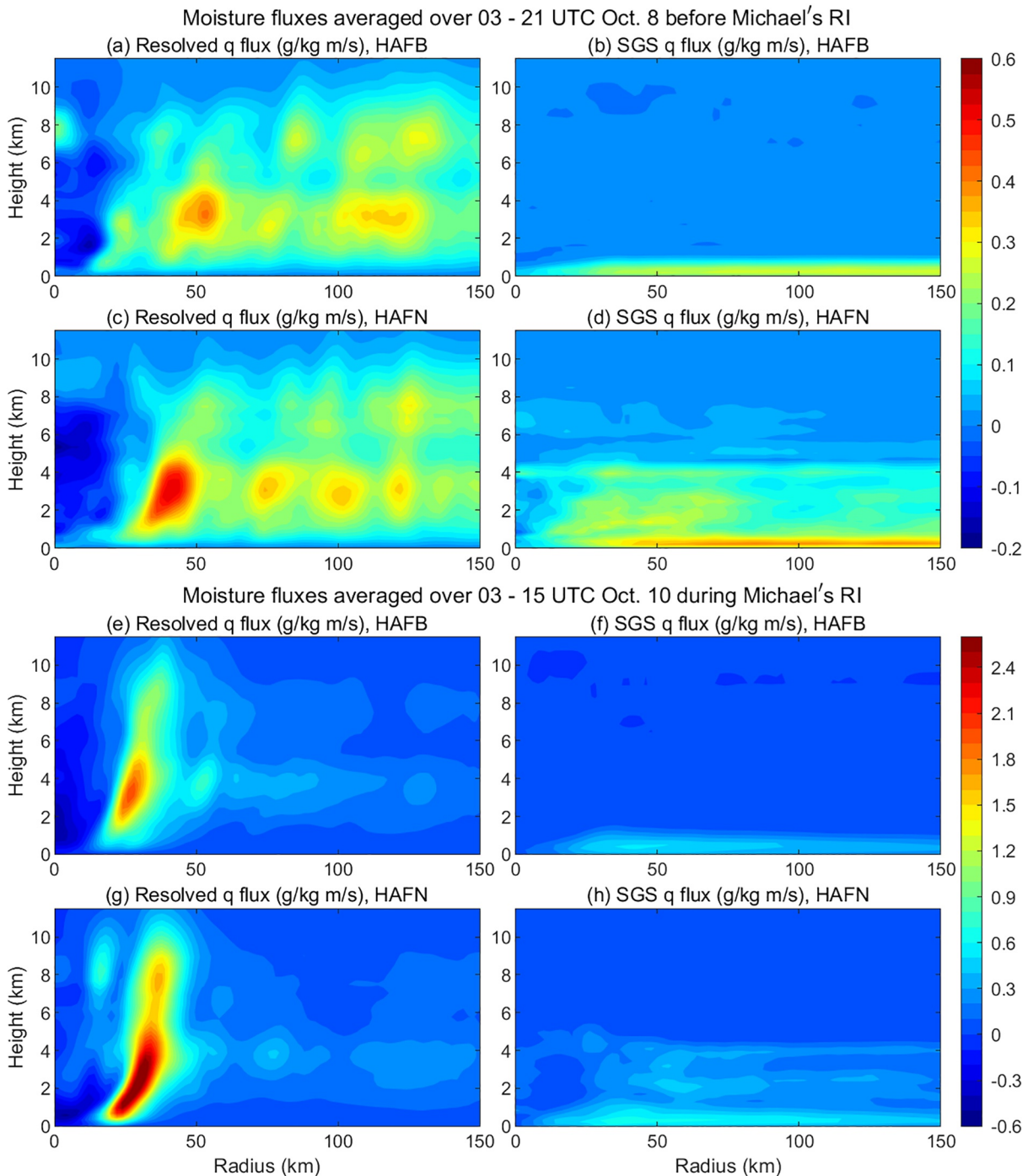


**Figure 13.** (a–d): Azimuthal-mean vertical moisture fluxes induced by the model-resolved and parameterized sub-grid scale (SGS) eddy processes averaged over the period of 03–21 UTC, October 8 before Michael's RI from the simulations by HAFB and HAFN, respectively. (e–h): The same as (a–d) but for the moisture fluxes averaged over the period of 03–15 UTC, October 10 during Michael's rapid intensification (RI).

## 6. Summary

The vertical SGS turbulent transport is an important process that needs to be appropriately parameterized in numerical prediction of TCs. In a TC environment, turbulence is no longer a flow feature only pertaining to the PBL, it can also be generated by the cloud processes aloft above the PBL. In particular, in the eye-wall and rainbands of a TC, there is no physical interface (such as an inversion) to separate the turbulence

generated within and above the PBL. How to remediate a conventional turbulent mixing scheme developed originally for non-TC conditions so that it can appropriately account for the turbulence within and above the PBL in the eyewall and rainbands is an important issue to address.

We found that the turbulent mixing scheme used in the HAFS-globalnest, a new multi-scale forecasting and analyses system for TC prediction, lacks the ability to represent the intense turbulent mixing in eyewall or rainband clouds. This problem results from the incorrect calculation of static stability using the BVF formula that is, only valid for the unsaturated atmosphere, and thus, it cannot account for the cloud-induced buoyancy in the eyewall and rainbands. From a parcel theory, we derived an expression of BVF for the saturated atmosphere containing multi-phase of water including vapor and liquid and solid hydrometeors. The offline calculations using the HAFS-globalnest model output show that the new formula of BVF for the saturated atmosphere substantially reduces the large stability bias estimated by the unsaturated BVF formula, which allows the turbulent mixing scheme to generate the appropriate eddy exchange coefficients in eyewall and rainband clouds. The analyses further show that the solid hydrometeors have a notable impact on the static stability of eyewall deep convection. Neglecting the effect of solid hydrometeors on static stability above the freezing level may lead to a poor parameterization of in-cloud turbulence and affect the fidelity of convection simulation in the eyewall.

We implemented the static stability correction in HAFS-globalnest and simulated 21 storms that include major CAT 3–5 hurricanes, weak CAT 1–2 hurricanes, and TS in the North Atlantic basin of 2016–2019 hurricane seasons, totaling 118 forecast cycles using the baseline HAFB and the HAFN. The comparison with the NHC best-track data show that HAFN outperforms HAFB in almost all forecasting measures of storm track, intensity, and structure. Specifically, the stability correction reduces the track forecasting error by  $\sim 15$  NM by the end of 5-days forecast, cuts the intensity forecasting error down to  $(-5, +5)$  KT compared with  $(-10, -20)$  KT by HAFB in 2–5 days forecast, improves the forecast of absolute maximum wind speed by  $[4, 5]$  KT in 2–3 days forecast, and reduces the negative biases of RMW by  $\sim (3, 6)$  n mi in 1–5 days forecast. These improvements suggest the importance of the parameterization of vertical turbulent transport above the PBL in the eyewall to the numerical prediction of TCs, in particular, to the correction of the negative intensity bias of HAFS-globalnest.

To better understand the role of eyewall turbulent transport in TC intensification, we compared and analyzed the simulations of Hurricane Michael (2018) by HAFB and HAFN. It shows that the vortex structure including the eyewall, asymmetric rainbands, and the moat between the eyewall and rainbands simulated by HAFN resembles more to that observed by the satellite than the one simulated by HAFB. HAFN also generates a stronger secondary overturning circulation and a more robust microphysical-dynamical interaction in the inner-core region during Michael's RI than HAFB. This manifests a strong dependence of vortex structure and mean secondary circulation on the parameterized in-clouds turbulent processes in the eyewall. It suggests that the intensification processes may be understood from the azimuthal-mean perspective.

The azimuthal-mean tangential wind budget analyses show that the positive tendency resulting from the radially inward transport of absolute vorticity by the mean radial inflow dominates the eddy correlation tendencies induced by the model-resolved asymmetric eddies and serves as a main mechanism for the vortex acceleration. In the HAFN simulation of Michael, the large positive tendency induced by the inward transport of absolute vorticity accelerates the tangential wind, leading to the increase of surface evaporation and radial convergence of moisture in the PBL, which in turn fosters stronger eyewall convection and causes the further increase of radial inflow. This kicks off a WISHE-like positive feedback leading to the RI of Michael. In contrast, the tendency induced by the inward transport of absolute vorticity in the HAFB simulation remains relatively small. The remnant positive tendency after compensating for the frictional dissipation is not sufficiently large to generate the needed acceleration of tangential wind to kick off the WISHE-like feedback mechanism. This result suggests that the mean eyewall convection must exceed a critical level so that the induced secondary overturning circulation can generate sufficiently large inward transport of absolute vorticity needed for vortex intensification.

The diagnoses of the vertical moisture transport induced by the model-resolved and SGS eddy processes show that the latter plays a key role in initiating the WISHE-like positive feedback underlying the RI. Without the SGS vertical moisture transport above the PBL in the eyewall, the moisture transport by the

model-resolved processes alone in the HAFB simulation is not sufficient to support the needed convection to kick off the WISHE-like positive feedback mechanism. The situation is different in the HAFN simulation in which the parameterized SGS vertical moisture transport above the PBL is comparable to that induced by the model-resolved processes before Michael's RI. It is the combined turbulent transport by the model-resolved and SGS processes that kicks off the WISHE-like positive feedback. It is in this context that the role of the SGS turbulent transport above the PBL in TC intensification is clear. It helps initiate the WISHE-like positive feedback underlying the RI that sets the intensification pathway for a developing vortex. Finally, we want to note although this mechanism appears to be robust at the current model resolution, it needs to be reevaluated as model resolution becomes sufficiently high to resolve large energy-containing turbulent eddies.

## Appendix A: BVF for the Unsaturated and Saturated Atmosphere

Static stability of the atmosphere may be measured by the vertical acceleration of an air parcel in its environment,  $a = g \left( \frac{\rho^e - \rho^p}{\rho^p} \right)$ , where  $\rho$  is the air density, superscripts "p" and "e" denote the air parcel and environment respectively hereafter. Applying the ideal gas law,  $p = \rho R_d T_v$ , where  $p$  is the air pressure,  $T_v$  is the virtual temperature, and  $R_d$  is the gas constant for dry air, the acceleration of an air parcel may be rewritten as  $a = g \left( \frac{T_v^p - T_v^e}{T_v^e} \right)$ , where we have used the adiabatic assumption  $p^p = p^e$ . Assuming that the air parcel at height  $z = 0$  is in an equilibrium, that is,  $T_v^p(0) = T_v^e(0)$ , for a small vertical displacement  $\delta z$ , one has:  $T_v^p = T_v^p(0) + \left( \frac{\partial T_v^p}{\partial z} \right) \delta z$  and  $T_v^e = T_v^e(0) + \left( \frac{\partial T_v^e}{\partial z} \right) \delta z$ . This yields  $a = -N^2 \delta z$ , where

$$N^2 = \frac{g}{T_v^e} \left( \frac{\partial T_v^e}{\partial z} - \frac{\partial T_v^p}{\partial z} \right), \quad (\text{A1})$$

is known as the Brunt-Väisälä frequency (BVF).

For the unsaturated atmosphere,  $-\left( \frac{\partial T_v^p}{\partial z} \right)$  may be replaced by the dry adiabatic lapse rate  $\Gamma_d = \left( \frac{g}{C_{pd}} \right)$ , where  $C_{pd}$  is the specific heat of dry air at constant pressure. Defining the virtual potential temperature as  $\theta_v = T_v \left( \frac{p_0}{p} \right)^{R_d/C_p}$ , where  $p_0$  is a reference pressure, then, applying it to the environment and taking its derivative with respect to height  $z$ , it is easy to show that Equation A1 may be rewritten as,

$$N^2 = \frac{g}{T_v^e} \left( \frac{\partial T_v^e}{\partial z} + \frac{g}{C_{pd}} \right) = \frac{g}{\theta_v^e} \frac{\partial \theta_v^e}{\partial z}. \quad (\text{A2})$$

For the saturated atmosphere, Equation A2 is no longer valid since  $-\left( \frac{\partial T_v^p}{\partial z} \right)$  deviates substantially from  $\Gamma_d$  owing to the latent heating release. In this case,  $N^2$  needs to be calculated directly from Equation A1, where an expression of  $T_v$  may be derived as follows.

$$\rho = \rho_d (1 + q_s + q_c) = \frac{p - E}{R_d T} (1 + q_t), \quad (\text{A3})$$

where  $\rho_d$  is the dry air density;  $q_s$ ,  $q_c$ , and  $q_t$  are the mixing ratios of the saturated water vapor, condensate (liquid and solid), and total water, respectively;  $E$  is the saturated water vapor pressure, which can be related to  $q_s$  as:  $q_s = \epsilon E / (p - E)$ , where  $\epsilon = \left( \frac{R_d}{R_v} \right)$  is the ratio of gas constant for dry air  $R_d$  to gas constant of water vapor  $R_v$ . Equation A3, then, can be rewritten as,  $p = \rho R_d T \left( 1 + \left( \frac{q_s}{\epsilon} \right) \right) / (1 + q_t)$ . From that, one may define  $T_v$  as,

$$T_v = T \frac{1 + (q_s/\epsilon)}{1 + q_t}. \quad (\text{A4})$$

with Equation A4, Equation A1 becomes,

$$N^2 = g \left\{ \left[ \frac{1}{T^e} \frac{\partial T^e}{\partial z} + \frac{1}{(\epsilon + q_s^e)} \frac{\partial q_s^e}{\partial z} - \frac{1}{(1 + q_t^e)} \frac{\partial q_t^e}{\partial z} \right] - \frac{T_v^p}{T_v^e} \left[ \frac{1}{T^p} \frac{\partial T^p}{\partial z} + \frac{1}{(\epsilon + q_s^p)} \frac{\partial q_s^p}{\partial z} - \frac{1}{(1 + q_t^p)} \frac{\partial q_t^p}{\partial z} \right] \right\}. \quad (\text{A5})$$

$\partial q_s / \partial z = q_s (1 + (q_s / \epsilon)) ((\partial E / \partial z) - (1/p)(\partial p / \partial z))$  in Equation A5 can be easily calculated from the Clausius–Clapeyron equation for the saturated atmosphere containing single type of hydrometeors (either liquid or solid). However, it is not easy to determine for the saturated atmosphere containing both liquid and solid hydrometeors. Here, we define  $E = \delta E_w + (1 - \delta) E_i$ , where  $\delta$  and  $1 - \delta$  are the ratios of liquid and solid hydrometeors to total hydrometeors;  $E_w$  and  $E_i$  are the saturated water vapor pressure associated with liquid and solid hydrometeors that satisfies  $(1/E_w)(\partial E_w / \partial T) = l_v / (R_v T^2)$  and  $(1/E_i)(\partial E_i / \partial T) = l_s / (R_v T^2)$ , respectively;  $l_v$  and  $l_s$  are the specific latent heat of vapourization and sublimation. Then,  $\partial E / \partial z$  may be rewritten as  $\partial E / \partial z = \delta (\partial E_w / \partial z) + (1 - \delta) (\partial E_i / \partial z) = l_m / (R_v T^2)$ , where  $l_m = (\delta E_w l_v + (1 - \delta) E_i l_s) / E$  is defined as the combined specific latent heat of vapourization and sublimation for mixed phase clouds. Here  $(E_w - E_i)(\partial \delta / \partial z)$  is assumed to be negligible compared to the other terms. Then,  $\partial q_s / \partial z$  may be rewritten as,

$$\frac{\partial q_s}{\partial z} = q_s \left( 1 + \frac{q_s}{\epsilon} \right) \left( \frac{l_m}{R_v T^2} \frac{\partial T}{\partial z} - \frac{1}{p} \frac{\partial p}{\partial z} \right). \quad (\text{A6})$$

Applying Equation A6 to the air parcel and environment, respectively, and inserting them into Equation A5, and utilizing the assumption that the total water of an air parcel is conserved during an adiabatic process, that is,  $\partial q_t^p / \partial z = 0$ , it yields,

$$N^2 = g \left\{ \left[ \left( 1 + \frac{l_m q_s^e}{R_d T^e} \right) \frac{1}{T^e} \frac{\partial T^e}{\partial z} - \frac{q_s^e}{\epsilon p^e} \frac{\partial p^e}{\partial z} - \frac{1}{(1 + q_t^e)} \frac{\partial q_t^e}{\partial z} \right] - \frac{T_v^p}{T_v^e} \left[ \left( 1 + \frac{l_m q_s^p}{R_d T^p} \right) \frac{1}{T^p} \frac{\partial T^p}{\partial z} - \frac{q_s^p}{\epsilon p^p} \frac{\partial p^p}{\partial z} \right] \right\}. \quad (\text{A7})$$

Applying the adiabatic assumption and hydrostatic balance  $\partial p^p / \partial z = \partial p^e / \partial z = -(p^e g) / (R_d T_v^e)$ , Equation A7 may be simplified as,

$$N^2 \approx g \left\{ \left[ \left( 1 + \frac{l_m q_s^e}{R_d T^e} \right) \frac{1}{T^e} \left( \frac{\partial T^e}{\partial z} + \Gamma_m \right) - \frac{1}{1 + q_t^e} \frac{\partial q_t^e}{\partial z} \right] \right\}, \quad (\text{A8})$$

where we have used the approximations  $(1 + (l_m q_s^e) / (R_d T^e)) / T^e \approx (T_v^p / T_v^e) (1 + (l_m q_s^p) / (R_d T^p)) / T^p$  and  $(q_s^e - q_s^p) g / (\epsilon R_d T_v^e) \approx 0$ . A key parameter in Equation A8 is the moist adiabatic lapse rate of temperature  $\Gamma_m = -(\partial T^p / \partial z)$ . While there are many rough estimates of  $\Gamma_m$  available in literature and textbooks, none of them considers the effect of multi-phase water (liquid and solid) on  $\Gamma_m$ . Here following Bohren and Albrecht (1998), we provide a derivation of  $\Gamma_m$  from the conservation of the total entropy of a saturated air parcel containing mixed phase hydrometeors, which may be expressed as,

$$\frac{\partial H^p}{\partial z} = 0 \quad H^p = M_d^p H_d^p + M_v^p H_v^p + M_w^p H_w^p + M_i^p H_i^p, \quad (\text{A9})$$

where  $M_d^p$ ,  $H_d^p$ ,  $M_v^p$ ,  $H_v^p$ ,  $M_w^p$ ,  $H_w^p$ ,  $M_i^p$ , and  $H_i^p$  are the mass and entropy of dry air, water vapor, liquid water, and solid water (ice, snow, and graupel) of an air parcel, respectively. For adiabatic processes, the total water mass and dry air mass are conserved, that is,  $\partial (M_v^p + M_w^p + M_i^p) / \partial z = 0$  and  $\partial M_d^p / \partial z = 0$ . Defining  $q_s = M_v / M_d$ ,  $q_w = M_w / M_d$ , and  $q_i = M_i / M_d$ , Equation A9 becomes,

$$\left( H_v^p - H_i^p \right) \frac{\partial q_s^p}{\partial z} + \left( H_w^p - H_i^p \right) \frac{\partial q_w^p}{\partial z} + \frac{\partial H_d^p}{\partial z} + q_s^p \frac{\partial H_v^p}{\partial z} + q_w^p \frac{\partial H_w^p}{\partial z} + q_i^p \frac{\partial H_i^p}{\partial z} = 0. \quad (\text{A10})$$

Further applying (a) the entropy change during water phase change,  $T^p (H_v^p - H_i^p) = l_f$ ,  $T^p (H_w^p - H_i^p) = l_f$ , where  $l_f$  is the specific latent heat of fusion; (b) the entropy change of ideal dry air and saturated water vapor,  $\partial H_d^p / \partial z = (C_{pd} / T^p) (\partial T^p / \partial z) - (R_d / (p^p - E^p)) (\partial (p^p - E^p) / \partial z)$ ,

$\partial H_v^p / \partial z = (C_{pv} / T^p) (\partial T^p / \partial z) - (R_v / E^p) (\partial E^p / \partial z)$ , which can be readily obtained from the first law of thermodynamics; and (c) the entropy change of liquid and solid hydrometeors,  $\partial H_w^p / \partial z = (C_w / T^p) (\partial T^p / \partial z)$ ,  $\partial H_i^p / \partial z = (C_i / T^p) (\partial T^p / \partial z)$ , where  $C_w$  and  $C_i$  are the specific heat of liquid and solid water, respectively, then, grouping all terms in Equation A10 containing  $\partial T^p / \partial z$  together, and using  $q_s = \epsilon E / (p - E)$ , Equation A10 can be simplified to,

$$\frac{l_s}{T^p} \frac{\partial q_s^p}{\partial z} + \frac{l_f}{T^p} \frac{\partial q_w^p}{\partial z} - \frac{R_d}{(p^p - E^p)} \frac{\partial p^p}{\partial z} + \frac{(C_{pd} + C_{pv} q_s^p + C_w q_w^p + C_i q_i^p)}{T^p} \frac{\partial T^p}{\partial z} = 0. \quad (\text{A11})$$

Applying Equation A6 to the air parcel and inserting it in the first term of Equation A11, it yields,

$$\left[ \frac{C_{pd} + C_{pv} q_s^p + C_w q_w^p + C_i q_i^p + \frac{(\epsilon + q_s^p) l_s l_m q_s^p}{R_d T^{p2}}}{T^p} \right] \frac{\partial T^p}{\partial z} + \frac{l_f}{T^p} \frac{\partial q_w^p}{\partial z} - \frac{(\epsilon + q_s^p) l_s q_s^p}{\epsilon T^p p^p} \frac{\partial p^p}{\partial z} - \frac{R_d}{(p^p - E^p)} \frac{\partial p^p}{\partial z} = 0. \quad (\text{A12})$$

Further applying  $\partial p^p / \partial z = \partial p^e / \partial z = -\rho^e g$ ;  $p^e = \rho^e R_d T_v^e$ ; the definition of  $T_v$ ; and  $q_s = \epsilon E / (p - E)$ , the last two terms of Equation A12 can be simplified as,  $-\frac{(\epsilon + q_s^p) l_s q_s^p}{\epsilon T^p p^p} \frac{\partial p^p}{\partial z} - \frac{R_d}{p^p - E^p} \frac{\partial p^p}{\partial z} \approx \frac{(1 + q_t^e) g}{T^e} \left( 1 + \frac{l_s q_s^p}{R_d T^p} \right)$ , where we have used the approximations  $1 \gg (q_s / \epsilon)$  and  $p \gg E$ . Then, from Equation A12, it is easy to show,

$$\Gamma_m = -\frac{\partial T^p}{\partial z} = \frac{g}{C_{pd}} \cdot \frac{\left( 1 + q_t^e \right) \left( 1 + \frac{l_s q_s^p}{R_d T^p} \right) + \frac{l_f}{g} \frac{\partial q_w^p}{\partial z}}{1 + \frac{C_{pv} q_s^p + C_w q_w^p + C_i q_i^p}{C_{pd}} + \frac{(\epsilon + q_s^p) l_s l_m q_s^p}{C_{pd} R_d T^{p2}}}. \quad (\text{A13})$$

with Equations A8 and A13, the static stability  $N^2$  of the saturated atmosphere that contains multi-phase water can be determined. However, the calculation is not as straightforward as Equation A2 for the unsaturated atmosphere because Equation A13 involves variables of both the air parcel and environment. In previous studies, such as Durran and Klemp (1982) and Bohren and Albrecht (1998), the variables of the air parcel and environment in their final formulae of  $N^2$  and  $\Gamma_m$  are not explicitly distinguished and are all treated as the environmental variables for calculation. We think it is important to understand the assumptions made for such a treatment. Recall that  $N^2$  by definition is a local variable rather than a global variable for an entire vertical column. Thus, an appropriate way to apply Equations A8 and A13 is to divide a vertical column of the atmosphere into a number of small segments based on the data points. For observational or numerical data, the segments can be naturally defined between the observational data points or model levels. Equations A8 and A13 are, then, applied to each data point along a vertical profile. In other words, the data points along a vertical profile are considered as a series of equilibrium points where the parcel's thermodynamic properties equal to those of environment, and an air parcel in each segment is assumed to follow an individual adiabatic process from its equilibrium. With this assumption, all parcel variables are taken their values at model grid points since each grid point is assumed as an equilibrium point, then, Equations A8 and A13 may be rewritten as,

$$N^2 \approx g \left\{ \left( 1 + \frac{l_m \bar{q}_s}{R_d \bar{T}} \right) \frac{1}{\bar{T}} \left( \frac{\partial \bar{T}}{\partial z} + \Gamma_m \right) - \frac{1}{(1 + \bar{q}_t)} \frac{\partial \bar{q}_t}{\partial z} \right\}, \quad (\text{A14})$$



$$\Gamma_m = \frac{g}{C_{pd}} \cdot \frac{\left(1 + \overline{q_t}\right) \left(1 + \frac{l_s \overline{q_s}}{R_d \overline{T}}\right) + \frac{l_f}{g} \frac{\partial \overline{q_w}}{\partial z}}{1 + \frac{C_{pv} \overline{q_s} + C_w \overline{q_w} + C_i \overline{q_i}}{C_{pd}} + \frac{\left(\epsilon + \overline{q_s}\right) l_s l_m \overline{q_s}}{C_{pd} R_d \overline{T}^2}}, \quad (\text{A15})$$

where overbar indicates the model-resolved variables at model grid points.

## Data Availability Statement

Data used in this study can be accessed at <http://vortex.ihrc.fiu.edu/download/HAFS/>.

## Acknowledgments

This work is supported by NOAA/HFIP under Grants NA16NWS4680029 and NA18NWS4680057 and National Science Foundation under Grant AGS-1822238. We are very grateful to the three anonymous reviewers for their constructive and insightful comments, which lead to the improvement of the paper.

## References

- Bender, M. A., Ginis, I., Tuleya, R., Thomas, B., & Marchok, T. (2007). The operational GFDL coupled hurricane–ocean prediction system and a summary of its performance. *Monthly Weather Review*, *135*, 3965–3989. <https://doi.org/10.1175/2007mwr2032.1>
- Bohren, C. F., & Albrecht, B. A. (1998). *Atmospheric thermodynamics* (p. 416). Oxford University Press.
- Bretherton, C. S., & Park, S. (2009). A new moist turbulence parameterization in the Community Atmosphere Model. *Journal of Climate*, *22*(12), 3422–3448. <https://doi.org/10.1175/2008JCLI2556.1>
- Businger, J. A., Wyngaard, J. C., Izumi, I., & Bradley, E. F. (1971). Flux-profile relationships in the atmospheric surface layer. *Journal of the Atmospheric Sciences*, *28*, 181–189. [https://doi.org/10.1175/1520-0469\(1971\)028<0181:fprita>2.0.co;2](https://doi.org/10.1175/1520-0469(1971)028<0181:fprita>2.0.co;2)
- Chen, J.-H., & Lin, S.-J. (2013). Seasonal predictions of tropical cyclones using a 25-km-resolution general circulation model. *Journal of Climate*, *26*, 380–398. <https://doi.org/10.1175/jcli-d-12-00061.1>
- Durran, D. R., & Klemp, J. B. (1982). On the effects of moisture on the Brunt-Väisälä frequency. *Journal of the Atmospheric Sciences*, *39*(2), 2152–2158. [https://doi.org/10.1175/1520-0469\(1982\)039<2152:OTEOMO>2.0.CO;2](https://doi.org/10.1175/1520-0469(1982)039<2152:OTEOMO>2.0.CO;2)
- Emanuel, K. A. (2003). Tropical cyclone. *Annual Review of Earth and Planetary Sciences*, *31*, 75–104. <https://doi.org/10.1146/annurev.earth.31.100901.141259>
- Giangrande, S. E., Collis, S., Straka, J., Protat, A., Williams, C., & Krueger, S. (2013). A summary of convective-core vertical velocity properties using ARM UHF wind profilers in Oklahoma. *Journal of Applied Meteorology and Climatology*, *52*, 2278–2295. <https://doi.org/10.1175/jamc-d-12-0185.1>
- Gopalakrishnan, S., Hazelton, A., & Zhang, A. J. (2021). Improving Hurricane boundary layer parameterization scheme based on observations. *Earth and Space Science*, *8*(3), e2020EA001422. <https://doi.org/10.1029/2020EA001422>
- Gopalakrishnan, S., Marks, F. D., Zhang, J. A., Zhang, X., Bao, J.-W., & Tallapragada, V. (2013). A study of the impact of vertical diffusion on the structure and intensity of tropical cyclones using the high-resolution HWRF system. *Journal of the Atmospheric Sciences*, *70*, 524–541. <https://doi.org/10.1175/jas-d-11-0340.1>
- Han, J., & Bretherton, C. S. (2019). TKE-based moist eddy-diffusivity mass-flux (EDMF) parameterization for vertical turbulent mixing. *Weather and Forecasting*, *34*, 869–886. <https://doi.org/10.1175/waf-d-18-0146.1>
- Han, J., Wang, W., Kwon, Y. C., Hong, S., Tallapragada, V., & Yang, F. (2017). Updates in the NCEP GFS cumulus convection schemes with scale and aerosol Awareness. *Weather and Forecasting*, *32*(5), 2005–2017. <https://doi.org/10.1175/waf-d-17-0046.1>
- Han, J., Witek, M., Teixeira, J., Sun, R., Pan, H.-L., Fletcher, J. K., & Bretherton, C. S. (2016). Implementation in the NCEP GFS of a hybrid eddy-diffusivity mass-flux (EDMF) boundary layer parameterization with dissipative heating and modified stable boundary layer mixing. *Weather and Forecasting*, *31*, 341–352. <https://doi.org/10.1175/waf-d-15-0053.1>
- Harris, L. M., & Lin, S.-J. (2013). A two-way nested global-regional dynamical core on the cubed-sphere grid. *Monthly Weather Review*, *141*, 283–306. <https://doi.org/10.1175/mwr-d-11-00201.1>
- Hazelton, A., Alaka, G. J., Jr., Cowan, L., Fischer, M., & Gopalakrishnan, S. (2021). Understanding the processes causing the early intensification of Hurricane Dorian through an ensemble of the Hurricane Analysis and Forecast System (HAFS). *Atmosphere*, *12*, 93. <https://doi.org/10.3390/atmos12010093>
- Hazelton, A., Zhang, X., Ramstrom, W., Gopalakrishnan, S., Marks, F. D., & Zhang, A. J. (2020). High-resolution ensemble HFV3 forecasts of Hurricane Michael (2018): Rapid intensification in shear. *Monthly Weather Review*, *148*, 2009–2032. <https://doi.org/10.1175/mwr-d-19-0275.1>
- Hazelton, A., Zhang, Z., Liu, B., Dong, J., Alaka, G., Wang, W., et al. (2021). 2019 Atlantic hurricane forecasts from the global-nested hurricane analysis and forecast system (HAFS): Composite statistics and key events. *Weather and Forecasting*, *36*, 519–538. <https://doi.org/10.1175/WAF-D-20-0044.1>
- Hogan, R. J., Grant, A. L. M., Illingworth, A. J., Pearson, G. N., & O'Connor, E. J. (2009). Vertical velocity variance and skewness in clear and cloud-topped boundary layers as revealed by Doppler lidar. *Quarterly Journal of the Royal Meteorological Society*, *135*, 635–643. <https://doi.org/10.1002/qj.413>
- Hong, S.-Y., & Pan, H.-L. (1996). Nonlocal boundary layer vertical diffusion in a Medium-Range Forecast model. *Monthly Weather Review*, *124*, 2322–2339. [https://doi.org/10.1175/1520-0493\(1996\)124<2322:nblvdi>2.0.co;2](https://doi.org/10.1175/1520-0493(1996)124<2322:nblvdi>2.0.co;2)
- Iacono, M. J., Delamere, J. S., Mlawer, E. J., Shephard, M. W., Clough, S. A., & Collins, W. D. (2008). Radiative forcing by long-lived greenhouse gases: Calculations with the AER radiative transfer models. *Journal of Geophysical Research*, *113*, D13103. <https://doi.org/10.1029/2008jd009944>
- Kaplan, J., Rozoff, C. M., DeMaria, M., Sampson, C. R., Kossin, J. P., Velden, C. S., et al. (2015). Evaluating environmental impacts on tropical cyclone rapid intensification predictability utilizing statistical models. *Weather and Forecasting*, *30*, 1374–1396. <https://doi.org/10.1175/waf-d-15-0032.1>

- LeMone, M. A., & Zipser, E. J. (1980). Cumulonimbus vertical velocity events in GATE. Part I: Diameter, intensity and mass flux. *Journal of the Atmospheric Sciences*, *37*, 2444–2457. [https://doi.org/10.1175/1520-0469\(1980\)037<2444:cvveig>2.0.co;2](https://doi.org/10.1175/1520-0469(1980)037<2444:cvveig>2.0.co;2)
- Lin, S.-J. (2004). A “vertically Lagrangian” finite-volume dynamical core for global models. *Monthly Weather Review*, *132*, 2293–2307. [https://doi.org/10.1175/1520-0493\(2004\)132<2293:avldc>2.0.co;2](https://doi.org/10.1175/1520-0493(2004)132<2293:avldc>2.0.co;2)
- Lorsolo, S., Zhang, J. A., Marks, F. D., & Gamache, J. (2010). Estimation and mapping of hurricane turbulent energy using airborne Doppler measurements. *Monthly Weather Review*, *138*, 3656–3670. <https://doi.org/10.1175/2010MWR3183.1>
- Marks, F. D., Black, P. G., Montgomery, M. T., & Burpee, R. W. (2008). Structure of the eye and eyewall of Hurricane Hugo (1989). *Monthly Weather Review*, *136*, 1237–1259. <https://doi.org/10.1175/2007mwr2073.1>
- Montgomery, M. T., & Smith, R. K. (2014). Paradigms for tropical cyclone intensification. *Australian Meteorological and Oceanographic Journal*, *64*, 37–66. <https://doi.org/10.22499/2.6401.005>
- Nolan, D. S., Moon, Y., & Stern, D. P. (2007). Tropical cyclone intensification from asymmetric convection: Energetics and efficiency. *Journal of the Atmospheric Sciences*, *64*, 3377–3405. <https://doi.org/10.1175/jas3988.1>
- Persing, J., Montgomery, M. T., McWilliams, J. C., & Smith, R. K. (2013). Asymmetric and axisymmetric dynamics of tropical cyclones. *Atmospheric Chemistry and Physics*, *13*, 12299–12341. <https://doi.org/10.5194/acp-13-12299-2013>
- Schubert, W. H., Wakefield, J. S., Steiner, E. J., & Cox, S. K. (1979). Marine stratocumulus convection. Part I: Governing equations and horizontally homogeneous solutions. *Journal of the Atmospheric Sciences*, *36*, 1286–1307. [https://doi.org/10.1175/1520-0469\(1979\)036<1286:mcpig>2.0.co;2](https://doi.org/10.1175/1520-0469(1979)036<1286:mcpig>2.0.co;2)
- Toepfer, F., Gall, R., Marks, F. D., & Rappaport, E. (2010). *Hurricane Forecast Improvement Program five year strategic plan* (p. 59). HFIP Doc. Retrieved from <http://www.hfip.org/documents/>
- Tyner, B., Zhu, P., Zhang, Gopalakrishnan, J. A. S., Marks, F., Jr., Tallapragada, V., & Tallapragada, V. (2018). A top-down pathway to secondary eyewall formation in simulated tropical cyclones. *Journal of Geophysical Research: Atmospheres*, *123*, 174–197. <https://doi.org/10.1002/2017JD027410>
- Wang, W., Sippel, J. A., Abarca, S., Zhu, L., Liu, B., Zhang, Z., et al. (2018). Improving NCEP HWRF simulations of surface wind and inflow angle in the eyewall area. *Weather and Forecasting*, *33*, 887–898. <https://doi.org/10.1175/waf-d-17-0115.1>
- Zhang, J. A., Kalina, E. A., Biswas, M. K., Rogers, R. F., Zhu, P., & Marks, F. D. (2020). A review and evaluation of planetary boundary layer parameterizations in Hurricane weather research and forecasting model using idealized simulations and observations. *Atmosphere*, *11*(10), 1091. <https://doi.org/10.3390/atmos11101091>
- Zhang, J. A., Marks, F. D., Montgomery, M. T., & Lorsolo, S. (2011). An estimation of turbulent characteristics in the low-level region of intense Hurricanes Allen (1980) and Hugo (1989). *Monthly Weather Review*, *139*, 1447–1462. <https://doi.org/10.1175/2010mwr3435.1>
- Zhang, J. A., Rogers, R. F., Nolan, D. S., & Marks, F. D. (2011). On the characteristic height scales of the hurricane boundary layer. *Monthly Weather Review*, *139*, 2523–2535. <https://doi.org/10.1175/mwr-d-10-05017.1>
- Zhu, P., Tyner, B., Zhang, J. A., Aligo, E., Gopalakrishnan, S., Marks, F. D., et al. (2019). Role of eyewall and rainband in-cloud turbulent mixing in tropical cyclone intensification. *Atmospheric Chemistry and Physics*, *19*, 14289–14310. <https://doi.org/10.5194/acp-19-14289-2019>